Biophysical *Journal*
Article

Biophysical Society

Constitutive Model of Erythrocyte Membranes with Distributions of Spectrin Orientations and Lengths

Zhe Feng,[1,2] Richard E. Waugh,[3] and Zhangli Peng[1,*]
[1]Department of Bioengineering, University of Illinois at Chicago, Chicago, Illinois; [2]Department of Aerospace and Mechanical Engineering, University of Notre Dame, Notre Dame, Indiana; and [3]Department of Biomedical Engineering, University of Rochester, Rochester, New York

ABSTRACT We present an analytical hyperelastic constitutive model of the red blood cell (erythrocyte) membrane based on recently improved characterizations of density and microscopic structure of its spectrin network from proteomics and cryo-electron tomography. The model includes distributions of both orientations and natural lengths of spectrin and updated copy numbers of proteins. By applying finite deformation to the spectrin network, we obtain the total free energy and stresses in terms of invariants of shear and area deformation. We generalize an expression of the initial shear modulus, which is independent of the number of molecular orientations within the network and also derive a simplified version of the model. We apply the model and its simplified version to analyze micropipette aspiration computationally and analytically and explore the effect of local cytoskeletal density change. We also explore the discrepancies among shear modulus values measured using different experimental techniques reported in the literature. We find that the model exhibits hardening behavior and can explain many of these discrepancies. Moreover, we find that the distribution of natural lengths plays a crucial role in the hardening behavior when the correct copy numbers of proteins are used. The initial shear modulus values we obtain using our current model (5.9–15.6 pN/μm) are close to the early estimates (6–9 pN/μm). This new, to our knowledge, constitutive model establishes a direct connection between the molecular structure of spectrin networks and constitutive laws and also defines a new picture of a much denser spectrin network than assumed in prior studies.

SIGNIFICANCE This work makes significant contributions to our understanding of the physical basis of red blood cell (RBC) elasticity. We present the first, to our knowledge, microstructure-based elastic model of RBC membranes that accounts for higher densities of spectrin indicated by recent proteomic analysis of RBC proteins, a distribution of spectrin natural lengths obtained from cryo-electron tomography, and the capacity for local cytoskeletal density changes. We show that for the higher spectrin densities indicated by proteomics, accounting for a distribution of molecular lengths in the resting state is essential for reproducing strain-hardening behavior exhibited by the RBC membrane in experiments.

INTRODUCTION

The mechanical properties of the membranes of red blood cells (RBCs or erythrocytes) have been extensively studied, but there remains a lack of integrated understanding from the molecular level to the continuum level. On one hand, empirical continuum constitutive laws have been well established, such as the ones described in the monograph by Evans and Skalak (1). In this approach, a two-dimensional hyperelastic constitutive model is derived from thermodynamics using invariants based on assumptions such as isotropy. In early work, Skalak et al. derived a strain energy function of red blood cell membrane based on the invariants of Green's strain tensor (2). Subsequently, to better separate the shear deformation and the area deformation, Evans and Skalak provided another strain energy function in terms of the area invariant $\alpha = \lambda_1\lambda_2 - 1$ and shear invariant $\beta = (\lambda_1/\lambda_2 + \lambda_2/\lambda_1 - 2)/2$, where λ_1 and λ_2 are the principal stretch ratios (1). For simplicity, the derivatives of free energy with respect to invariants were assumed to be constants and, as such, define the shear modulus and mean stress resultant (isotropic tension) in the material. In this formulation, the area modulus was defined as the second derivative of the free energy with respect to area, and this was also assumed to be a constant.

Subsequently, the accumulation of experimental evidence indicates that the shear modulus and area modulus are certainly not constants, as would be expected based on the highly nonlinear behaviors of biopolymers with mixed entropic and energetic contributions to free energy (3–5). Ironically, Dimitrakopoulos found that the original Skalak

Submitted March 6, 2020, and accepted for publication October 15, 2020.
*Correspondence: zhpeng@uic.edu
Editor: Ana-Suncana Smith.
https://doi.org/10.1016/j.bpj.2020.10.025

law (2), which was supplanted by thermodynamically based models, does a reasonable job of explaining the discrepancy in the shear modulus measurements due to its hardening behavior (6), but connections between such models and molecular events are not defined.

From the molecular perspective, several coarse-grained molecular dynamics models have been developed to study the cytoskeletal cortex of RBCs, but no systematic effort has been made to extract the mechanical properties of these coarse-grained molecular dynamics models to reconstruct corresponding continuum strain-dependent constitutive models that could be used for whole-cell simulations of in vivo biological processes or in vitro experiments. One exception is the work of Dao et al., who derived shear and areal moduli for small deformations using a spectrin-level model based on the virial stress (7). Another exception is the work of Svetina et al. (8), who used an energy method based on a random network of ideal springs to make macroscopic predictions of membrane behavior, including micropipette aspirations, and derived expressions for the deformation dependence of the area and shear moduli, although explicit stress-strain relationships were not derived. Thus, although several microscopic models of RBC membranes have been developed, including spectrin-level models (9–11), with few exceptions, these have not been linked to mechanical behaviors at large deformation via continuum models. In addition, there are recent proteomic data from two independent sources (12,13) showing that whereas the stoichiometry of spectrins and junctional complex proteins are consistent with earlier estimates, copy numbers of RBC proteins such as spectrin are two- to threefold higher than well-accepted values in the literature (14). The predictions of any molecularly based model of red cell membrane behavior need to be re-examined in light of these new data.

In this study, we present a novel, to our knowledge, constitutive description for arbitrarily large deformation that is based on, and connects directly to, spectrin-level behavior as a worm-like chain. In addition, we also derive a simplified version of the constitutive law and give the corresponding analytical solution of the pressure-length relation in micropipette aspiration. Our approach accounts for two important characteristics not found in earlier constitutive models; namely, it exhibits strain-hardening behavior, and it allows for local changes in cytoskeletal density. This latter feature is in keeping with fluorescence imaging experiments showing that the cytoskeleton density does change significantly when cells are aspirated into micropipettes (15), becoming compressed near the pipette entrance and expanded near the tip of the membrane projection. We will explore the effect of the area change on the aspiration curve and measured shear modulus using the microstructure-based model. With microstructure-based strain hardening and cytoskeletal area change, good comparisons with our experiments and those in the literature are demonstrated.

METHODS

Constitutive model of the RBC cytoskeleton with orientation distributions of spectrins

We consider the relationship between the molecular free energy of the molecules of the cytoskeletal network and the free energy per unit area of the skeleton. We follow the development of Discher and colleagues (9), which was based on a molecular network model developed by Boey et al. (16). The membrane skeleton was treated as a triangular elastic network in which the springs connecting network nodes have the characteristics of an elastic, worm-like polymer modeled after erythrocyte spectrin. The energy of the triangular network took the form (9)

$$E_{net} = \sum_{bonds} \left[V_{eff}(s) + C/\tilde{A} \right], \tag{1}$$

where $\tilde{A}$ is the area per molecule and C is a coefficient preventing network collapse. The attractive potential ($V_{eff}(s)$) of the "bonds" that represent the spectrin molecules was derived from the force-extension relationship of a worm-like chain (WLC) with both ideal and divergent behavior (17). The approximate interpolation formula of the WLC potential (17) for a bond with node-to-node distance s and maximal separation s_{max} is

$$V_{eff}(s) = \frac{k_B T s_{max}}{4p} \left(\frac{s}{s_{max}} \right)^2 \frac{3 - 2\, s/s_{max}}{1 - s/s_{max}}, \tag{2}$$

where p is the persistence length of the chain segments, k_B is Boltzmann's constant, and T is the absolute temperature. The corresponding force of the effective WLC potential is given as

$$f(s) = -\frac{\partial V_{eff}}{\partial s} = -\frac{k_B T}{p} \left[\frac{1}{4(1 - s/s_{max})^2} - \frac{1}{4} + s / s_{max} \right]. \tag{3}$$

Discher and colleagues applied these molecular models to obtain predictions both for the distribution of skeletal density in pipette aspirated cells and for the projection length of a biconcave disk being aspirated into a micropipette at different pressures (9). There are three unknown molecular parameters in the model: the maximal molecular length s_{max}, the persistence length p, and the area coefficient C. Writing the molecular lengths relative to their stress-free natural length (s/s_o) and imposing the condition that the system must be in a minimal energy state at rest, one can solve for one of these parameters (C) in terms of the other two, leaving two coefficients to adjust to vary the mechanical stiffness of the network, p and $\lambda_{max} = s_{max}/s_o$.

Taking s_o as the resting molecular length, the molecular extension (s/s_o) is

$$\frac{s}{s_0} = |\boldsymbol{F} \cdot \boldsymbol{t}_0| = \sqrt{\boldsymbol{t}_0 \cdot \boldsymbol{C} \cdot \boldsymbol{t}_0},$$

where $\boldsymbol{t}_0$ is the filament unit orientation in the reference configuration,

$$\boldsymbol{C} = \boldsymbol{F}^T \boldsymbol{F} = \begin{bmatrix} \lambda_1^2 & 0 \\ 0 & \lambda_2^2 \end{bmatrix},$$

is the right Cauchy-Green deformation tensor, and $\boldsymbol{F}$ is the deformation gradient. The molecular extension s/s_o is related to the material stretch ratios by

$$\left(\frac{s}{s_0} \right)_i^2 = \lambda_1^2 \cos^2\theta_{0,i} + \lambda_2^2 \sin^2\theta_{0,i}, \tag{4}$$

where $\theta_{0,i} = i\pi/n,\ i \in (1, n)$ is the angle between the molecular vector for orientation i and the principal axis of extension in the resting state. The energy per unit area must be summed over molecular orientations. Note that in this formulation, n is the number of distinct molecular orientations in the resting state, not the number of elements in a network unit. For example, in a regular hexagonal array, $n = 3$, but in a random network, $n \to \infty$.

In Appendix B in the Supporting Materials and Methods, we show the detailed derivation of the stress resultants from the energy. The resulting constitutive equations for the skeleton take the form

$$\tau_1^{sk} = c_\beta \left[\frac{2}{n} \frac{\lambda_1}{\lambda_2} \sum_{i=1}^{n} \left(\cos^2\theta_{0,i}\, P_i\left(\frac{s}{s_o}\right)\right) - \frac{c_\alpha}{\lambda_1^2\lambda_2^2}\right]. \quad (5)$$

and

$$\tau_2^{sk} = c_\beta \left[\frac{2}{n} \frac{\lambda_2}{\lambda_1} \sum_{i=1}^{n} \left(\sin^2\theta_{0,i}\, P_i\left(\frac{s}{s_o}\right)\right) - \frac{c_\alpha}{\lambda_1^2\lambda_2^2}\right], \quad (6)$$

where

$$c_\alpha = \frac{6\lambda_{max}^2 - 9\lambda_{max} + 4}{(\lambda_{max} - 1)^2}, \quad (7)$$

$$c_\beta = \frac{k_B T \rho_0}{8(p/s_0)\lambda_{max}}, \quad (8)$$

and

$$P_i(s/s_o) = \frac{6\lambda_{max}^2 - 9\lambda_{max}(s/s_o)_i + 4(s/s_o)_i^2}{\left(\lambda_{max} - (s/s_o)_i\right)^2}. \quad (9)$$

Note that c_α is functionally related to λ_{max}, meaning that there are just two freely adjustable material coefficients (c_β and λ_{max}) in this model. The stress resultants can also be written in terms of shear and isotropic components

$$\tau_s^{sk} = \frac{\tau_1^{sk} - \tau_2^{sk}}{2}$$

$$= \frac{c_\beta}{2}\left\{ \left(\frac{\lambda_1}{\lambda_2} - \frac{\lambda_2}{\lambda_1}\right)\frac{1}{n}\sum_{i=1}^{n} P_i(s/s_o) + \left(\frac{\lambda_1}{\lambda_2} + \frac{\lambda_2}{\lambda_1}\right)\ \frac{1}{n}\sum_{i=1}^{n}\left[P_i(s/s_o)\left(\cos^2(\theta_{0,i}) - \sin^2(\theta_{0,i})\right)\right]\right\}, \quad (10)$$

and

$$\tau_a^{sk} = \frac{\tau_1^{sk} + \tau_2^{sk}}{2} = c_\beta \left[\frac{1}{n\,\lambda_1\lambda_2} \sum_{i=1}^{n} P_i(s/s_o) - \frac{c_\alpha}{(\lambda_1\lambda_2)^2}\right]. \quad (11)$$

The expression for τ_s^{sk} can be used to express the dependence of the shear modulus μ on extension as

$$\mu = \frac{\partial w}{\partial \beta} = \frac{2\tau_s \lambda_1^2\lambda_2^2}{\lambda_1^2 - \lambda_2^2} = c_\beta \lambda_1\lambda_2 \left[\frac{1}{n}\sum_{i=1}^{n} P_i(s/s_o) + \left(\frac{\lambda_1^2 + \lambda_2^2}{\lambda_1^2 - \lambda_2^2}\right)\ \frac{1}{n}\sum_{i=1}^{n} P_i(s/s_o)\cos(2\theta_{0,i})\right]. \quad (12)$$

An important reference point for comparison with other theoretical developments is the value of the modulus at the resting state μ_0. Taking the limit at constant area for $\lambda_1 \cong 1 + \varepsilon$ and $\lambda_2 \cong 1 - \varepsilon$, $\varepsilon \to 0$, we obtain

$$\mu_0 = c_\beta \left[c_\alpha + \frac{3\lambda_{max}^2 - \lambda_{max}}{4(\lambda_{max} - 1)^3}\right] = \frac{k_B T \rho_0}{8(p/s_0)\lambda_{max}} \left[\frac{6\lambda_{max}^2 - 9\lambda_{max} + 4}{(\lambda_{max} - 1)^2} + \frac{3\lambda_{max}^2 - \lambda_{max}}{4(\lambda_{max} - 1)^3}\right]. \quad (13)$$

This expression is identical to one obtained previously by Dao et al. (7) for the specific case of $n = 3$. After substituting $x_0 = 1/\lambda_{max} = s_o/s_{max}$, recognizing that for a triangular network $\rho_0 = 2\sqrt{3}/s_0^2$, and applying algebraic manipulation, we find

$$\mu_0 = \frac{\sqrt{3} k_B T}{4 p s_{max} x_0}\left[\frac{3}{4(1 - x_0)^2} - \frac{3}{4} + 4x_0 + \frac{x_0}{2(1 - x_0)^3}\right]. \quad (14)$$

Note that

$$\frac{1}{\lambda_{max}}\left[\frac{6\lambda_{max}^2 - 9\lambda_{max} + 4}{(\lambda_{max} - 1)^2} + \frac{3\lambda_{max}^2 - \lambda_{max}}{4(\lambda_{max} - 1)^3}\right] = \frac{3}{4(1 - x_0)^2} - \frac{3}{4} + 4x_0 + \frac{x_0}{2(1 - x_0)^3}.$$

Remarkably, no assumptions about n were made in deriving Eq. 14, demonstrating that it is in fact accurate for all n with the same chain density.

Similarly, from the definition of area modulus $K^{sk} \equiv (\partial \tau_\alpha^{sk}/\partial\alpha)_\beta$ and as detailed in Appendix C in the Supporting Materials and Methods, the area modulus can be expressed as the following forms

$$K^{sk} = \frac{c_\beta}{2n(1 + \alpha)^2}\left[\sum_{i=1}^{n} \left(\frac{s}{s_0}\right)_i^3 \frac{3\lambda_{max}^2 - \lambda_{max}\left(\frac{s}{s_0}\right)_i}{\left(\lambda_{max} - \left(\frac{s}{s_0}\right)_i\right)^3}\right] + \frac{2c_\beta c_\alpha}{(1 + \alpha)^3}. \quad (15)$$

There are two forms of special interest. One is the isotropic case $\lambda_1 = \lambda_2 = s_i/s_0 = x = \sqrt{\alpha + 1}$,

$$K_{iso}^{sk} = c_\beta \left[\frac{2c_\alpha}{x^6} + \frac{1}{2x}\left(\frac{3\lambda_{max}^2 - x\lambda_{max}}{(\lambda_{max} - x)^3}\right)\right], \quad (16)$$

and the other is the limit of no deformation at the resting state $(s/s_0)_i \to 1$,

$$K_0^{sk} = c_\beta \left(2c_\alpha + \frac{3\lambda_{max}^2 - \lambda_{max}}{2(\lambda_{max} - 1)^3} \right). \tag{17}$$

Comparing Eq. 17 with Eq. 13, we find that the initial area modulus is twice the initial shear modulus, $K_0^{sk} = 2\mu_0$.

Simplified shear stress expression

For specific molecular orientations, a simplified expression can be derived to approximate the material behavior to facilitate analytical solutions to certain problems, such as micropipette aspiration. As detailed in Appendix B in the Supporting Materials and Methods, the shear stress resultant in Eq. 10, if the area is incompressible, can be approximated as

$$\tau_s^{sk} = \frac{2c_\beta}{3x_0} \left[c_0 + c_1(\lambda_1 - 1) + \frac{\lambda_1}{4(1 - \lambda_1 x_0)^2} \right], \tag{18}$$

where $c_0 = \frac{-1}{4(1-x_0)^2}$ and

$$c_1 = \frac{48x_0^4 - 153x_0^3 + 171x_0^2 - 71x_0 + 1}{4(x_0 - 1)^3}.$$

The shear modulus is given as

$$\mu = \frac{2\tau_s^{sk}}{\lambda_1^2 - \lambda_2^2} = \frac{4c_\beta}{3x_0(\lambda_1^2 - \lambda_2^2)} \left[c_0 + c_1(\lambda_1 - 1) + \frac{\lambda_1}{4(1 - \lambda_1 x_0)^2} \right]. \tag{19}$$

This equation also works for arbitrary $n > 2$. The detailed derivation and the case of area compressible cytoskeleton can be found in Appendix B in the Supporting Materials and Methods.

Constitutive model of RBC cytoskeleton with natural length distributions of spectrin

When we derived the expressions of the shear stress and energy function, we applied a single value for the natural end-to-end length s_o in the unstressed state. Recent tomographic studies demonstrate that the resting end-to-end distance of spectrin is not single valued but distributed over some range (18). In this case, we postulate that the energy of the skeleton and corresponding force resultants can be considered to be a superposition of networks with different resting end-to-end distances, weighted according to the frequency at which a given end-to-end distance occurs (at rest). In this case, the shear stress becomes

$$\tau_s^{sk} = \sum_i \varphi_i \tau_{s,i}^{sk}, \tag{20}$$

where φ_i is the fractional occurrence of a given end-to-end distance $s_{o,i}$. Cryo-electron microscopy (cryo-EM) data (18) show that for mouse erythrocytes, the initial length distribution is given as $\mathbf{s}_0 = [20, 30, 40, 50, 60, 70, 80, 90, 97]$ nm, with frequencies of $\mathbf{f} = [1, 17, 30, 38, 19, 17, 6, 1, 1]$. Then the fractional weight is $\boldsymbol{\varphi} = [0.00769, 0.13077, 0.23077, 0.29231, 0.14615, 0.13077, 0.046154, 0.00769, 0.00769]$. We can also write

$$\mu_0 = \sum_i \varphi_i \mu_{0,i}, \quad \mu = \sum_i \varphi_i \mu_i, \tag{21}$$

where $\mu_{0,\mathrm{i}} = (k_B T \rho_0 / 8(p / s_{0,i})\lambda_{max,i})[(6\lambda_{max,i}^2 - 9\lambda_{max,i} + 4/(\lambda_{max,i} - 1)^2) + (3\lambda_{max,i}^2 - \lambda_{max,i}/4(\lambda_{max,i} - 1)^3)]$, $\lambda_{max,i} = s_{max}/s_{0,i}$, and μ_i is given in Eq. 12 for specific $s_{0,i}$. Note that the maximal contour length s_{max} is assumed to be the same for all chains regardless of $s_{0,i}$.

Recent efforts have successfully localized junctional complexes on the red cell membrane using super-resolution microscopy (19), but because this approach requires sparse labeling, not all junctions are labeled, and interjunctional distances cannot be reliably determined. For example, the length distributions in this super-resolution imaging study were calculated as counts/μm^2, and the summation of the total counts in their figures gives $\sim$110 junctions/μm^2. This is much lower than the value of $\sim$730 junctions/μm^2 estimated from proteomic data (13) and even significantly lower than the traditional number of $\sim$270 junctions/μm^2 (14).

Analysis of micropipette aspiration

Closed form solution using an analytical model with the simplified constitutive model

Using the simplifying approximation in Eq. 18, a closed form prediction for the aspirated projection length of the cell as a function of aspiration pressure can be obtained. The cell deformation is approximated as the formation of a cylinder plus hemispherical cap from an infinite membrane plane (Fig. 1 *A*; (1)). For each projection length, the corresponding meridional tension at the pipette tip $\tau_{1,tip}^{sk}$ is determined, and this in turn is directly related to the predicted aspiration pressure $R_p \Delta P = 2\tau_{1,tip}^{sk}$. In this way, a prediction for the projection length as a function of aspiration pressure is generated, in this case from the equilibrium equation in cylindrical coordinates of the flat membrane

$$\tau_1^{sk} - \tau_2^{sk} + r\frac{d\tau_1^{sk}}{dr} = 0. \tag{22}$$

In the limit as $r \to \infty$, we take $\tau_1^{sk} \to 0$. In this case, the stress at the tip $\tau_{1,tip}^{sk}$ can be obtained by integrating Eq. 22,

$$\tau_{1,tip}^{sk} = \int_{R_p}^{\infty} \frac{2\tau_s^{sk}}{r} dr, \tag{23}$$

where $\tau_s^{sk} = (\tau_1^{sk} - \tau_2^{sk})/2$. To evaluate the integral, we make the simplifying assumption that the cytoskeleton is laterally incompressible. From the definition of the principle stretch, we have $\lambda_2 = r/r_0$. In the area incompressible case, we can relate the instantaneous position of a material element r to is initial location in the undeformed plane r_0 by equating the areas: $\pi r_0^2 = \pi(r^2 + 2L_p R_p - R_p^2)$. This implies $\lambda_1 = \frac{r_0}{r} = \sqrt{(r^2 + 2L_p R_p - R_p^2)/r^2}$. At the lower limit of the integration, $r = R_p$, we have $\lambda_L = \lambda_1 | r = R_p = \sqrt{2L_p/R_p}$. With these simplifications, recognizing that $(dr/d\lambda_1) = (\lambda_1 \mathrm{r}/1 - \lambda_1^2)$ and using the expression for the stress given in Eq. 18, we evaluate the integral (Eq. 23):

$$\tau_{1,tip}^{sk} = \frac{4c_\beta}{3x_0} \left[D_0(x_0) + D_1(x_0)\lambda_L + D_2(x_0)\ln\left(\frac{\lambda_L + 1}{2}\right) + D_3(x_0)\ln\left(\frac{1 - x_0}{1 - x_0\lambda_L}\right) + \frac{D_4(x_0)}{1 - x_0\lambda_L} \right], \tag{24}$$

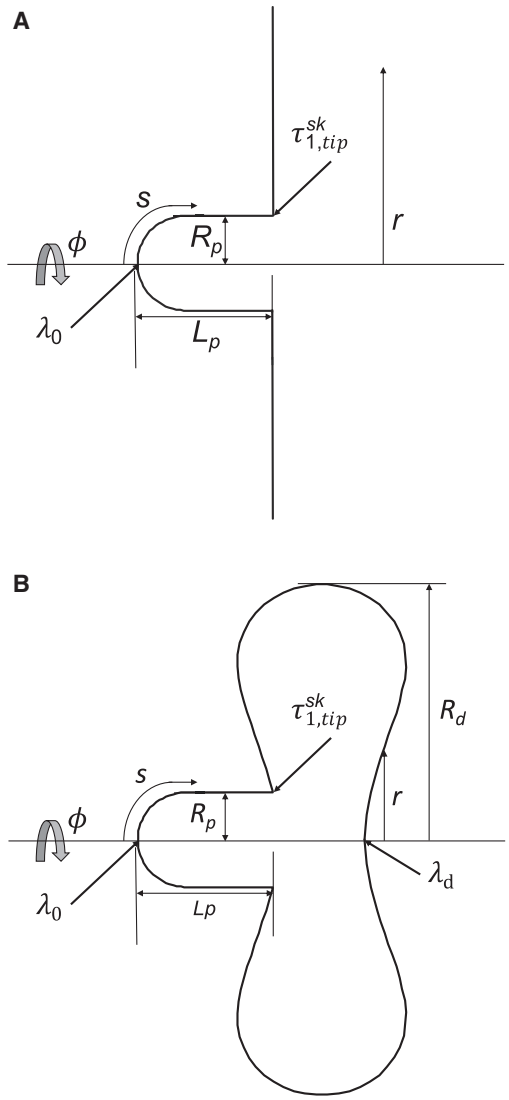

FIGURE 1 (*A*) The analytical model for analyzing micropipette aspiration by assuming an infinite flat membrane outside the pipette is shown. (*B*) The ODE model for analyzing micropipette aspiration by assuming a biconcave shape outside the pipette is shown. A cross section of the axisymmetric cell contour used in the analysis showing coordinate directions is given. Key experimental parameters are the pipette radius R_p and the length of the aspirated membrane projection L_p. The meridional distance along the surface is s, and the radial coordinate is r. The radius of the outer disk R_d is calculated to conserve total surface area. Integration proceeds from the tip of the projection and the center of the disk outside the pipette. The starting stretch ratios λ_0 and λ_d are found such that the membrane stress resultant at the pipette tip $\tau^{sk}_{1,\,tip}$ is continuous and the total mass of the membrane-associated cytoskeleton is conserved.

where

$$\lambda_L = \sqrt{2L_p/R_p},$$

$$D_0(x_0) = \frac{-1}{4(1+x_0)^2(1-x_0)^2 x_0} - c_1,$$

$$D_1(x_0) = c_1,$$

$$D_2(x_0) = -\frac{x_0^2+1}{4(1+x_0)^2(1-x_0)^2} - c_1,$$

$$D_3(x_0) = \frac{x_0}{2(1+x_0)^2(1-x_0)^2},$$

and

$$D_4(x_0) = \frac{1}{4(1-x_0)^2}.$$

Because $R_p\Delta P = 2\tau^{sk}_{1,tip}$, we have the aspiration pressure ΔP vs. length L_p relation as

$$R_p\Delta P = \frac{8c_\beta}{3x_0}\left[D_0(x_0) + D_1(x_0)\lambda_L + D_2(x_0)\ln\left(\frac{\lambda_L+1}{2}\right) + D_3(x_0)\ln\left(\frac{1-x_0}{1-x_0\lambda_L}\right) + \frac{D_4(x_0)}{1-x_0\lambda_L}\right]. \quad (25)$$

Effect of natural length distributions of spectrin

With φ_i as the fractional weight of contributions for the end-to-end distance $s_{0,i}$, we have

$$R_p\Delta P = \sum_i\left\{\varphi_i\frac{8c_{\beta,i}}{3x_{0,i}}\left[D_0(x_{0,i}) + D_1(x_{0,i})\sqrt{\frac{2L_p}{R_p}} + D_2(x_{0,i})\ln\left(\frac{\sqrt{2L_p/R_p}+1}{2}\right) + D_3(x_{0,i})\ln\left(\frac{1-x_{0,i}}{1-x_{0,i}\sqrt{2L_p/R_p}}\right) + \frac{D_4(x_{0,i})}{1-x_{0,i}\sqrt{2L_p/R_p}}\right]\right\}, \quad (26)$$

where $c_{\beta,i} = k_B T\rho_0 x_{0,i}/8(p/s_{0,i})$ and $x_{0,i} = s_{0,i}/s_{max}$. Note that the maximal contour length s_{max} is assumed to be the same for all chains regardless of $s_{0,i}$.

Effect of adhesion energy between cell membranes and pipette walls

In a previous study (8), we have provided evidence of an attractive energy between the cell membrane and the micropipette, σ_{ap}. The effect of such an attractive interaction is to shift the predicted curves for L_p/R_p as a function of ΔPR_p along the horizontal axis. Effectively, this transforms $L_p/R_p = f(\Delta PR_p)$ to $L_p/R_p = f(\Delta PR_p + \sigma_{ap})$. We introduce σ_{ap} as a fitted constant for a given pipette on a given day of experiments.

Effect of cytoskeletal area change

We cannot calculate the distribution of cytoskeletal area change analytically because of mathematical difficulties, but if the cytoskeletal area change of

the flat membrane is assumed to be uniform, a modified analytical solution can be obtained as

$$R_p\Delta P = \frac{8c_\beta}{3x_0'}\left[D_0' + D_1'\lambda_L' + D_2'\ln\left(\frac{\lambda_L'+1}{2}\right) + D_3'\ln\left(\frac{1-x_0'}{1-x_0'\lambda_L'}\right) + \frac{D_4'}{1-x_0'\lambda_L'}\right] + 2T_\infty, \quad (27)$$

where detailed expressions for the coefficients can be found in Appendix C in the Supporting Materials and Methods.

Numerical solution using an ODE model with the general constitutive model

For the general expressions (Eqs. 5 and 6), we use a numerical approach to solve an ordinary differential equation (ODE) model to obtain predictions for the projection length as a function of aspiration pressure for a micropipette-aspirated biconcave cell (Fig. 1 *B*). We denote the principal stretches and stress resultant in the meridional direction as λ_1 and τ_1^{sk} and in the circumferential as λ_2 and τ_2^{sk}. By symmetry, we see that the principal stretch ratios at the tip of the membrane projection in the pipette λ_0, and the center of the disk opposite the pipette λ_d must be isotropic. For a given cell shape (projection length L_p and outer biconcave disk diameter R_d), we find values for λ_0 and λ_d that satisfy the conditions that the meridional tension at the tip of the pipette $\tau_{1,tip}^{sk}$ is continuous and the total mass of the membrane cytoskeleton is conserved (see Appendix A for details of this ODE model in the Supporting Materials and Methods).

Experimental measurements

The projection length of a portion of the red cell membrane aspirated into a micropipette was measured as a function of the aspiration pressure. Measurements were obtained on three different days using large (~0.85 μm inside diameter) and small (~0.56 μm inside diameter) micropipettes. Cells were obtained from human donors by simple finger stick under a protocol approved by the Office of Human Subject Protection at the University of Rochester. Cells were suspended in phosphate-buffered saline with 4% v/v of fetal bovine serum to avoid attachments between the cells and glass surfaces. Micropipettes were formed from glass capillaries using a Kopf microelectrode puller and a custom-made microforge. Micropipettes were filled by capillarity with buffer matching the cell suspension buffer, then connected via a continuous, bubble-free water pathway to a water-filled manometer. Zero pressure was set by adjusting the height of the manometer reservoir until suspended particles were motionless in the pipette lumen. Aspiration pressures were applied by adjusting the height of the reservoir using a micrometer with a resolution of 0.01 mm. Cells were observed using an inverted microscope with a 100× oil immersion objective and monochromatic illumination (480 nm). The experiments were recorded using standard video, and the length of the projection as a function of aspiration pressure was measured from the recordings. For each day of experiments, approximately eight cells were measured using the same pressure sequence, and the projection lengths at each pressure were averaged.

RESULTS

We first present results using a single value of resting end-to-end distances s_0 for spectrin to illustrate the general behaviors of the model and then introduce a distribution of resting end-to-end distances and demonstrate the importance of having such a distribution to better approximate actual cell behavior.

Parameter selection and stress-strain comparisons

An important advantage of our approach is the ability to see how changing specific characteristics of the molecular network affect the behavior of the membrane in deformation. Some examples of this are shown in Fig. 2. In the native membrane, the orientation of the network elements appears to be random. Thus, an important question to address is how increasing the number of different molecular orientations in the resting state affects the model predictions. This is shown in Fig. 2 *A* for a simple uniaxial extension ($\tau_2 = 0$). For small forces and extension, even a very small number of initial molecular orientations provides a prediction consistent with more complex expressions, but for large extensions, significant differences in the predictions emerge (Fig. 2 *B*). This implies that the number of distinct molecular orientations in the resting state only affects membrane behavior when molecular extensions approach their maximum. Estimates of accuracy for different numbers of molecular orientations are summarized in Appendix D in the Supporting Materials and Methods. For example, for $n = 3$, errors in the calculated stress exceed 5% when extensions are greater than 70% of λ_{max}, whereas for $n = 6$, extensions can be up to 90% of λ_{max} before errors greater than 5% are observed. Similar results were obtained for purely shear deformation (constant skeleton area). As might be expected, results for isotropic expansion of the skeleton showed no dependence on the number of molecular orientations included in the calculations (data not shown). In these examples, the maximal end-to-end distance was set to 200 nm, the persistence length was 25 nm, $s_0 = 75$ nm, and the molecular density was $2200/\mu m^2$.

Dependencies of the predicted stress resultants on molecular density ρ_0, persistence length p, and resting molecular length s_0 are straightforward because these only appear in the coefficient c_β, which multiplies the entire expression for the stress resultant (Eqs. 5 and 6). Thus, if the ratio of p/s_0 is doubled, the stress resultants for the corresponding stretch ratios are halved, and conversely, if the density of molecules is doubled, the stress resultants are doubled. The dependence of the model predictions on the maximal stretch ratio λ_{max} is more complex, but, generally, the stress resultant rises more quickly with extension for smaller values of λ_{max} and increases asymptotically as the extension approaches λ_{max} (Fig. 2, *C* and *D*). Interestingly, at higher extensions, normalizing the stretch ratio to λ_{max} collapses the prediction to a single curve (Fig. 2 *D*). Similar behaviors are exhibited for pure shear deformation.

It is also of interest to understand how the resistance to deformation as reflected in the material constants μ (shear modulus) and K (area modulus) vary with membrane deformation. We have already shown that the ratio of K/μ is 2.0 for small deformations relative to the resting state. This ratio changes substantially, however, as the membrane deforms

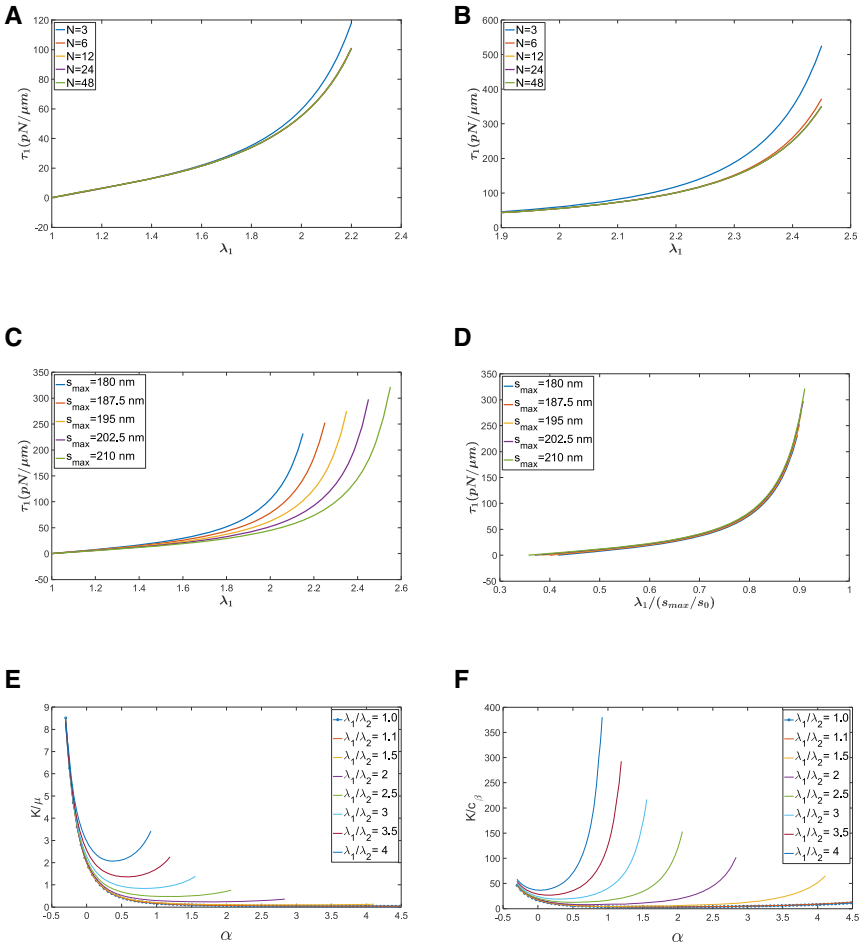

FIGURE 2 (*A*) Stress resultant τ_1 as a function of stretch for a uniaxial extension ($\tau_2 = 0$), $\rho_0 = 2200/\mu m^2$, $p = 25$ nm, $s_{max} = 200$ nm, and $s_0 = 75$ nm. For relatively modest extensions, the stress resultant has little dependence on the number of molecular orientations selected. (*B*) For large extensions, differences in the predicted stress resultant are found for fewer than 12 molecular orientations, but for $n \geq 12$, there is less than a 1% difference in the calculated values when the extension is 95% of its maximum. This is shown for $\lambda_{max} = 2.6$ but true for all values tested. (*C*) Increasing λ_{max} decreases the corresponding stress resultant. (*D*) As extensions approach the maximum, the curves collapse to a single prediction when expressed as a fraction of λ_{max}, indicating that τ_1 could be approximated by a single function of λ_1/λ_{max}. (*E*) The ratio of the area modulus *K*/shear modulus μ is 2.0 in the resting state but increases with compression and decreases, then increases with expansion. (*F*) The area modulus increases with compression and decreases with extension until the maximal molecular extension is approached. To see this figure in color, go online.

(Fig. 2 *E*). Indeed, both moduli vary significantly with membrane expansion. The variation in the area modulus K is shown in Fig. 2 *F*, and the variation in μ is shown in Appendix D (Fig. S7) in the Supporting Materials and Methods. Note that when the membrane is extended (increasing λ_1/λ_2), the resistance to dilation increases more rapidly because of the nonlinear increase in resistance to stretch as the maximal stretch ratio is approached.

Comparison of the stresses (Fig. 3 *A*) and shear modulus (Fig. 3 *B*) obtained using the full model (Eqs. 10 and 12) and the simplified formula (Eqs. 18 and 19) show good agreement over a wide range of extensions.

Effects of natural length distributions of spectrins

A recent study using tomographic imaging of intact red cells revealed that there is a distribution of end-to-end distances for spectrin molecules in the undeformed cytoskeleton (18). The reported distribution is reproduced in Fig. 4 *A*. Even though large values of $s_{0,i}$ occur rarely, they can have a significant impact on stress-strain behavior at larger extensions because of the singularity in molecular force as a function of extension when molecular lengths (s) approach s_{max}. This is illustrated in Fig. 4 *B*, where the dependence of the force resultant (τ_1) on extension is shown for three different but similar distributions, truncated at different values for s_0. The distributions with larger values for s_0 exhibit the greatest strain-stiffening behavior. Contributions from each individual value of s_0 in the distribution are shown for both small (Fig. 4 *C*) and large (Fig. 4 *D*) extensions.

Comparison of the prediction with micropipette aspiration experiments: analytical models

We consider three versions of the analytical models in comparison to experimental measurements. In the first version, we assume a single value for s_0 and fit s_0 and pipette adhesion energy σ_{ap} by least-squares regression with a fixed persistence length p and a fixed maximal molecular length s_{max}. We plotted three fits in Fig. 5 *A*. The best-fit values (*black curve* in Fig. 5 *A*) were $s_0 = 59.25$ nm and $\sigma_{ap} = 10.17$ pN/μm for fixed $p = 25$ nm, $s_{max} = 200$ nm, and $\rho_0 = 2200$ molecules/μm^2. This version of the model does not show obvious hardening unless a small $s_{max} = 140$ nm and an extremely large $p = 60$ nm is used (*red curve* in Fig. 5 *A*). This is due to the high density of spectrin we

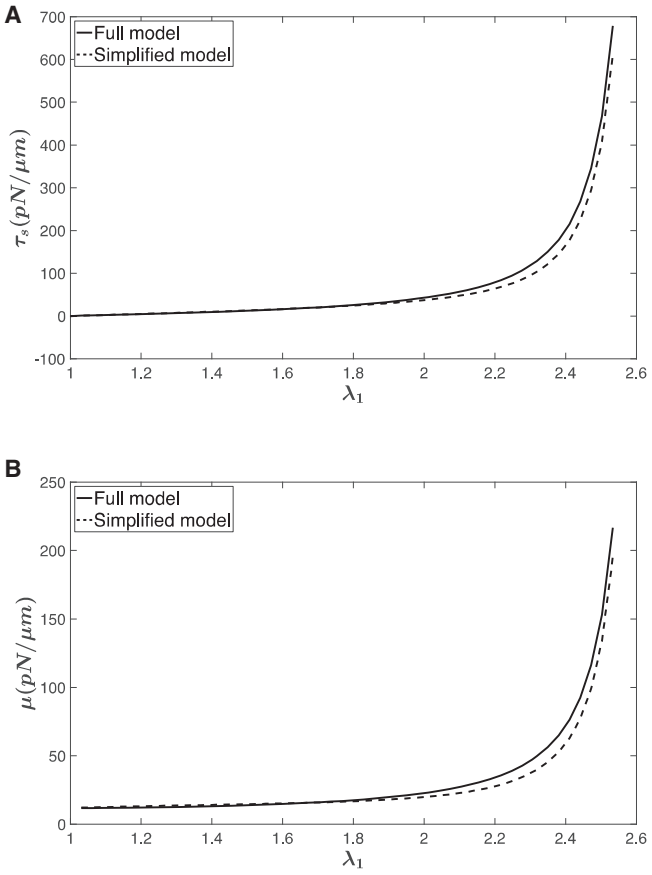

FIGURE 3 Comparison of the stress-strain curves and shear modulus between the full model (Eqs. 10 and 12) and the simplified model (Eqs. 18 and 19). Values for the other parameters used in the calculations: $\rho_0 = 2200/\mu m^2$, $p = 25$ nm, $s_{max} = 200$ nm, $s_0 = 75$ nm. (*A*) Shear stress resultant (area incompressible) is given. (*B*) Shear modulus (area incompressible) is given.

used based on proteomic data (2200 molecules/μm^2) (12,13). If we use earlier estimates of chain density calculated from a triangular network with an edge length of 75 nm, i.e., $\rho_0 = 2\sqrt{3}/s_0^2 = 616$ molecules/μm^2, it shows hardening at $s_{max} = 173$ nm and $p = 25$ nm (*cyan curve* in Fig. 5 *A*). Although this result is appealing from the perspective that we observe the expected strain hardening for more reasonable molecular characteristics, the underlying molecular assumptions are inconsistent with recent proteomic results (13). Next, we consider the case in which the values of s_0 are fixed but distributed according to electron microscopic tomography (Fig. 4 *A*; (18)). In this case, we consider three different fixed values for $p = 10$, 15, and 25 nm, and the values of σ_{ap} and s_{max} were determined from least-squares regression (Fig. 5 *B*). Increased persistence length p gives smaller fitted s_{max} and more obvious hardening behavior. Finally, we take into account the possibility that the density of the network may change locally when it is deformed. The ODE model with the general constitutive model (see Comparison of the Prediction with Micropipette Aspiration Experiments: ODE Model) predicts a net compression of the skeleton in the region of the membrane outside the pipette. In keeping with this finding, we postulate an average compression of up to ~0.65% in the membrane plane outside the pipette. We considered three cases with compressions of 0.0, 0.35, and 0.65%. With fixed $p = 25$ nm, we obtained s_{max} and σ_{ap} from the fit (Fig. 5 *C*). When the compression of the cytoskeleton outside the pipette is larger, we obtain smaller s_{max} (and larger μ_0). This implies that allowing redistribution of skeletal density to the membrane portion outside the pipette reduces the appearance of strain hardening (indicated by a downward curvature to the fitted curve) such that smaller values of s_{max} are required to achieve the level of strain hardening (downward curvature) exhibited by the data.

Comparison of the prediction with micropipette aspiration experiments: ODE model

We then apply the ODE model, described in Appendix A in the Supporting Material, to solve the micropipette aspiration numerically by considering the more realistic cell shape shown in Fig. 1 *B* and employing the full constitutive model (Eqs. 5 and 6) instead of the simplified one. In Fig. 6, *A* and *B*, we show the effects of varying the maximal molecular length s_{max} or the persistence length p on the predictions for micropipette aspiration experiments. The initial molecular lengths $s_{0,i}$ were distributed as shown in Fig. 4 *A*. We observe that both constants affect the slope of the predicted curve, implying that it is possible to compensate for changes in one parameter with changes in the other. On the other hand, although the persistence length p only changes the slope, the maximal molecular length s_{max} changes both the slope and the curvature of the predicted curve. Introduction of the adhesive energy between the cell membrane and the micropipette, σ_{ap}, enables fitting of the data with a range of value pairs for p and s_{max}. This is illustrated in Fig. 7, in which predicted curves based on three different pairs of values show comparable agreement with the data for each of the 3 days of experiments. In Fig. 7, *A* and *C*, the pipette diameter was 1.12 μm, and in Fig. 7 *B*, the diameter was 1.7 μm. For the fitting procedure, the density of molecules on the surface was set to 2200 molecules/μm^2, based on proteomic measurements indicating ~300,000 tetramers per cell (12,13) and using an average cell area of ~135 μm^2. The distribution of s_0 values was fixed according to Fig. 4 *A*. The value of s_{max} was set at a constant value (140, 160, and 200 nm), and least-squares regression was performed with two free parameters: p and σ_{ap}. Depending on the value chosen for s_{max}, different values for p and σ_{ap} were obtained. The value of σ_{ap} is subject to significant measurement uncertainty because although changes in L_p can be measured very accurately, uncertainty in the location of the pipette tip can lead to errors in its absolute magnitude, and these errors contribute directly to the value of σ_{ap}. Therefore, changes in the value of σ_{ap} between different experiments

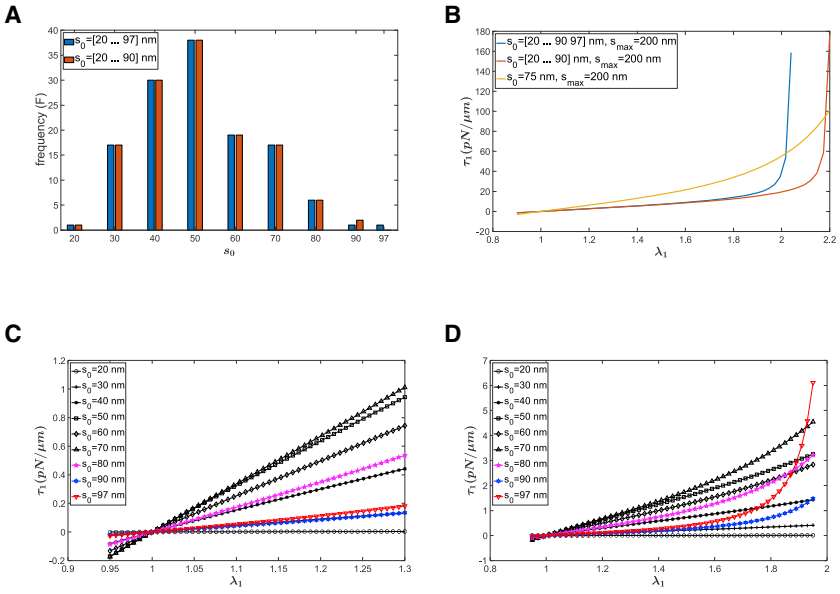

FIGURE 4 Effect of natural length distributions of spectrin. (*A*) Distributions of natural length from cryo-EM measurements (18) are shown. (*B*) Stress resultant τ_1 as a function of stretch for two distributions and a single natural length is given. (*C*) The contributions of each natural length to the total stress resultant τ_1 are shown. (*D*) The same as (*C*) is shown, but for larger stretch. Values for the other parameters used in the calculations: $\rho_0 = 2200/\mu m^2$, $p = 25$ nm, $s_{max} = 200$ nm. To see this figure in color, go online.

do not necessarily reflect differences that have physical significance. The value of the persistence length p, on the other hand, is of interest because it reflects a molecular property that contributes directly to macroscopic cell behavior. The relationship between the value chosen for s_{max} and the best-fit value for p is given in Fig. 7 *D*, in which the corresponding initial shear modulus is shown for each pair of p and s_{max}. The initial shear modulus μ_0 increased from 5.9 to 15.6 pN/μm with increasing s_{max}. The goodness of fits as reflected by the sum of squared residuals in Fig. 7 for different values of persistence length and maximal length is summarized in Appendix E in the Supporting Materials and Methods.

DISCUSSION

Derivation of a constitutive model based on molecular parameters facilitates an understanding of how molecular attributes affect membrane deformability. Key molecular characteristics include the density of spectrin on the membrane in the resting state ρ_0, the molecular persistence length p, the molecular lengths in the resting network s_0, and the maximal molecular extension s_{max}. In the model, the density and the persistence length appear explicitly only in the coefficient c_β, which is directly proportional to the magnitude of the stress for a given deformation. Consequently, the membrane modulus is expected to increase in direct proportion to spectrin density and inversely to the persistence length. In a previous study, a direct proportionality between the membrane shear modulus and the density of spectrin on the membrane has been documented (20), and this is consistent with the formulation we have developed here.

Best-fit values for the persistence length p in our experiments range from 10 to 50 nm. The highest values correspond to the lowest values for s_{max} (Fig. 7 *D*), the highest degree of strain hardening, and the smallest initial shear modulus (~5.9 pN/μm). Previously reported values for persistence length fall into the lower end of this range. For single molecules or intact cytoskeletons separated from the bilayer in solution, estimates of persistence length range from 10 to 25 nm (21,22). The persistence length for molecules constrained to remain near the membrane surface might be expected to be slightly smaller or up to 25% larger, based on estimates of the effects of confinement on this characteristic (23). Although the highest values we obtain are above this range, this might be expected given the constraints on spectrin conformation because of multiple membrane attachments. For an intermediate value of p around 25 nm, the fitted s_{max} is around 145 nm and the corresponding initial shear modulus $\mu_0 = 9.37$ pN/μm. For the smallest value of p around 8.5 nm, the fitted s_{max} is around 200 nm and the corresponding initial shear modulus $\mu_0 = 15.6$ pN/μm, but this case shows very limited hardening for the size of the aspiration lengths studied here.

Strain hardening and the distribution of resting molecular lengths

An important characteristic of the red cell cytoskeleton is strain hardening. In addition to evidence based on determination of the shear modulus using techniques that impose different magnitudes of strain, the pipette aspiration data reported here also show evidence of this in a downward curvature of the data for larger extensions (Fig. 7). Strain hardening is expected for models based on worm-like chain theory because these molecules become asymptotically stiff as they approach their maximal extension. However, the magnitude of the stretch ratios at which this behavior occurs

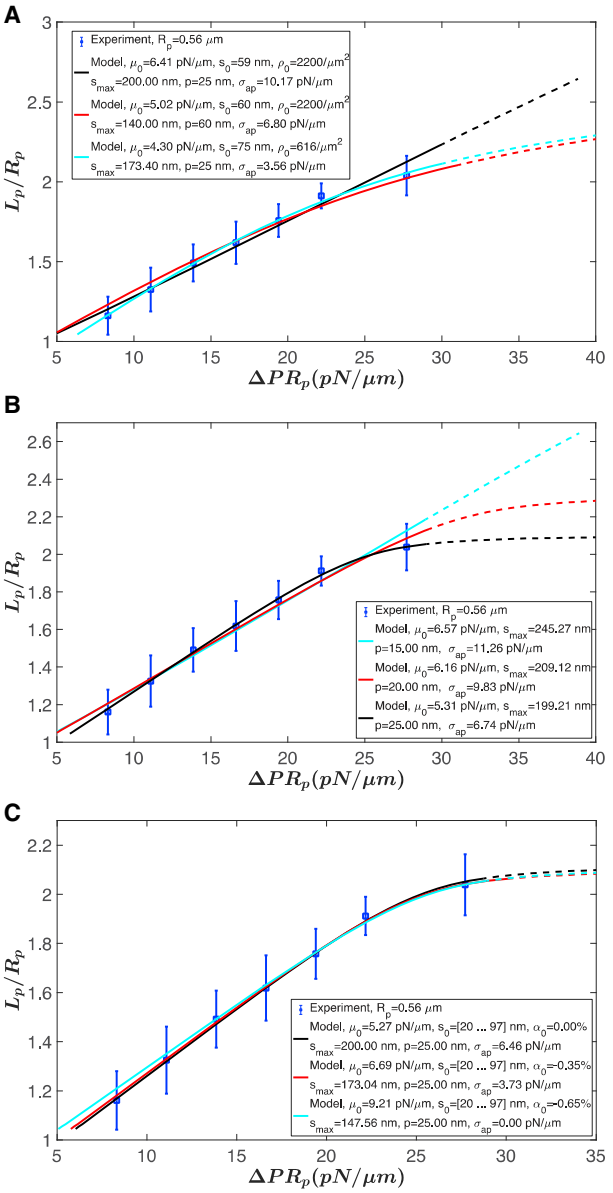

FIGURE 5 Comparison of the analytical model predictions with experimental data. (*A*) Fits with one global natural length without area change are shown. (*B*) Fits with distributed natural lengths (Fig. 4 *A*) without area change ($\rho_0 = 2200/\mu m^2$) are shown. (*C*) Fits with distributed natural lengths (Fig. 4 *A*) with an assumed uniform area change α_0 on the flat membrane outside the pipette ($\rho_0 = 2200/\mu m^2$) are shown. Dashed curves show the predictions beyond the experimental range. However, it should be noted that such lengths are not accessible experimentally because at longer extensions, folds begin to appear in the membrane, resulting in membrane shapes that are not amenable to analysis. Error bars for experimental data are shown as blue vertical lines. To see this figure in color, go online.

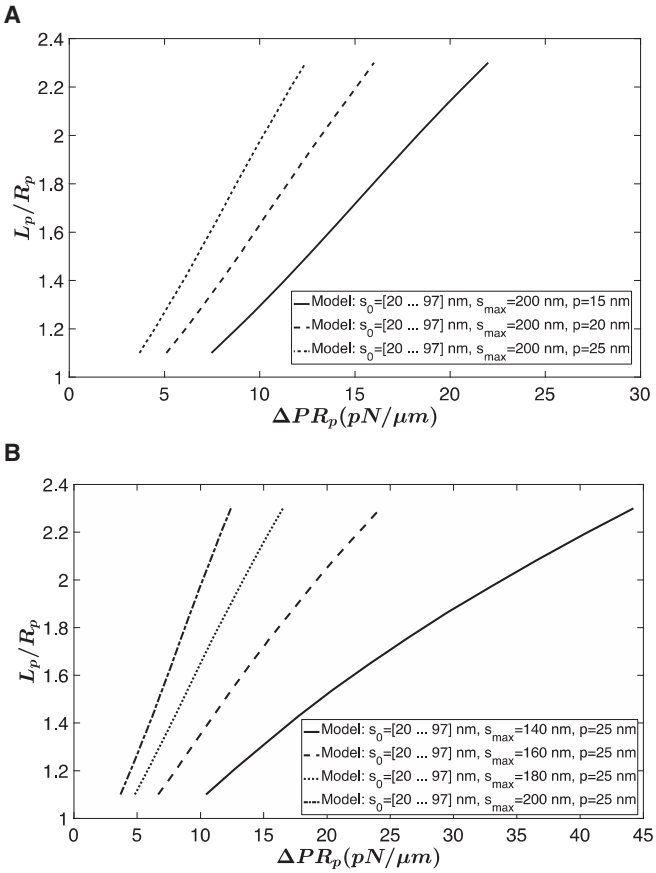

FIGURE 6 Sensitivity of model predictions to parameter values. (*A*) Effect of persistence length p is shown. (*B*) Effect of contour length s_{max} is shown. Increasing either p or s_{max} leads to increases in the length of the projection at a given aspiration pressure.

depends critically on the ratio of s_0 to s_{max}. Values for the fully extended lengths of spectrin tetramers (s_{max}) are based on rotary-shadowed electron micrographs, which indicated a maximal end-to-end distance of 180–200 nm (24,25). The resting length s_0 is typically calculated from estimates of spectrin density and the relationship between density and s_0 in triangular networks: $\rho_0 = 2\sqrt{3}/s_0^2$. It is important to appreciate the implications of recent proteomic and ultrastructural findings on these values (12,13,18). Until recently, estimates of the number of spectrin molecules on the cell surface were based on density analysis of polyacrylamide gels, which put the number of spectrin tetramers on the surface of a cell at 80,000–120,000 (14). This corresponds to a density of 600–900/μm^2 and implies that s_0 ranges from 60 to 75 nm. To our knowledge, all existing molecular models of the red cell cytoskeleton assume resting molecular lengths of ~70 nm. However, recent studies using more modern proteomic techniques put the number of tetramers much higher, ~300,000 per cell or ~2200 tetramers/μm^2 (12,13). This density corresponds to a value of s_0 of ~40 nm for a triangular network. This much-lower resting s_0 will have significant influence on the predictions of existing molecular models.

In relation to strain hardening, the value of $s_0 = 40$ nm implies that maximal molecular extensions in a network could approach a stretch ratio of 4.5–5.0 before significant worm-like stiffening would be observed. In this case, molecular models based on uniform networks would not predict the downward curvature that is evident in the micropipette

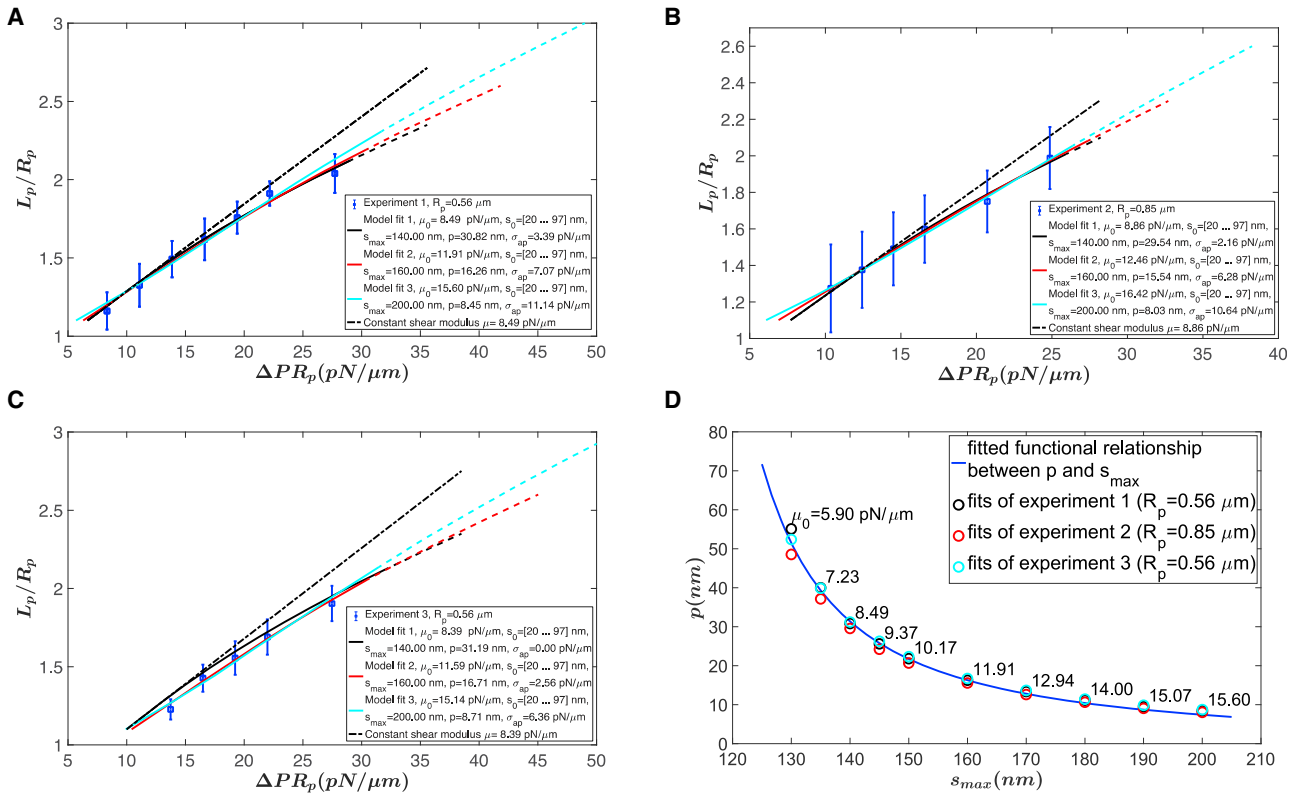

FIGURE 7 Comparison of the ODE model predictions with experimental data. Three different experiments are shown. (*A*) Experiment 1 with $R_p = 0.56$ μm, (*B*) experiment 2 with $R_p = 0.85$ μm, and (*C*) experiment 3 with $R_p = 0.56$ μm are shown. (*D*) Given a value for s_{max}, there is a unique value of p that matches the slope of the data for all three experiments. The relationship between p and s_{max} is shown as the solid line: $p = c_1(6 - 9c_2/s_{max} + 4c_2^2/s_{max}^2)/(s_{max}/c_2 - 1)^2$, where $c_1 = 0.0275$ and $c_2 = 101.85$. The corresponding initial shear modulus for experiment 1 is shown at each point. Dashed curves show the predictions beyond the experimental range. Error bars for experimental data are shown as blue vertical lines. The database can be found at: https://datadryad.org/stash/share/6ghOC1on3URHVUT55ACqW4W3PgB4TDKefVBDk-7FWKM. To see this figure in color, go online.

aspiration data. This dilemma is solved by recent tomographic evidence that end-to-end distances of tetramers in the resting state are not uniform (18). Accounting for this distribution, our molecular-based constitutive model leads to predictions of strain stiffening for extensions of ~2.0, and results in model predictions for pipette aspiration behavior much closer to what is observed. Additionally, if one reverses the calculation and estimates resting state density from the reported distribution of molecular lengths (using the relationship $\rho_0 = 2\sqrt{3}/s_0^2$ for triangular networks and performing a weighted sum over the values of s_0), one obtains a density of 1740/μm^2, a value in excellent agreement with densities based on proteomic results. This last point is strong validation for using both the distributed values for s_0 and the higher densities of spectrin indicated by the proteomic measurements.

Literature values for shear modulus

Values reported for the red cell membrane shear modulus in the literature differ significantly. For example, in micropipette aspiration experiments, in which the cell experiences moderate deformation, the shear modulus was measured as values (6–9 pN/μm) (26) or 4.2 pN/μm (27). The shear modulus measured using optical tweezers to stretch red blood cells and produce small deformations was 2.5 pN/μm (28,29), although some other measurements using optical tweezers gave a shear modulus of 5.7 pN/μm (30), 11.1–30 pN/μm (31), or 200 pN/μm (32). In addition to direct measurements of shear modulus, computational modeling studies also required a small shear modulus (~2.5 pN/μm) to predict the resting biconcave shape and the correct stomatocyte-discocyte-echinocyte shape transition (4,33,34). The ability of different constitutive laws to match experimental measurement are compared in several studies (6,35), but most do not account for strain-hardening behavior. Estimates based on membrane fluctuation measurements (36,37) or tank-treading phenomena (5,38,39), both of which involve relatively small deformations, also tend to produce smaller values. In one interpretation of thermal fluctuation experiments, the shear modulus appears to be very small or almost zero (36,37), whereas experiments on tank treading give a range of shear moduli from 2.81 to 8.95 pN/μm depending on the deformation (5). Although differences in experimental approaches and associated measurement uncertainties as well as different approximations

and methods of interpretation likely account for much of the differences in literature values, the strain stiffening captured using the microstructure-based model we present here may also help explain those differences. The value of the modulus in Eq. 21 approximately triples when the stretch ratio increases from 1.0 to 1.4 for $s_{max} = 140$ nm (Fig. 8). Consistent with this, tank-treading experiments showed that the shear modulus can be tripled when the stretch ratio increases from 1.2 to 1.64 as shown in Fig. 8, although the absolute value of the shear modulus is at least twofold lower than those extracted from micropipette aspiration using this model.

The original analysis of micropipette aspiration, which did not consider strain hardening or cytoskeletal density changes, gave a prediction for the relationship between projection length and aspiration pressure: $R_p \Delta P = \mu/R_p[2L_p/R_p - 1 + \ln(2L_p/R_p)]$. Using this approach, the calculated shear modulus was in the range of 6–9 pN/μm (1,26). Our current analysis shows that failing to account for strain hardening results in an overestimate of the initial shear modulus because it reflects an "averaged" value of the increasing shear modulus with deformation. On the other hand, our analysis also shows that failing to account for local changes in skeletal density leads to underestimation of the shear modulus because the constraint of constant density leads to higher shear stresses at the same macroscopic deformation (projection length) (Fig. 5 *C*). Therefore, these two effects tend to compensate for each other such that the initial shear modulus values we obtain using our current model (5.9–15.6 pN/μm) are not much different than early estimates (6–9 pN/μm).

Values obtained using the simplified models

The simplified models we have derived vastly reduce the computational costs for analyzing experimental data. However, this simplicity comes with some loss of consistency for the molecular coefficients. The approximate model without cytoskeletal area change shows stronger strain stiffening and appears to match two of the three experimental data sets with high accuracy (Fig. 5). It is important to note, however, that maintaining constant cytoskeletal density introduces an important constraint on the deformation, and this accounts for the increased strain stiffening for this model. Indeed, in Fig. 5 *C*, increasing the assumed cytoskeletal area change for the simplified model results in less hardening. From other experimental evidence, it is clear that local changes in density do occur when the membrane is deformed.

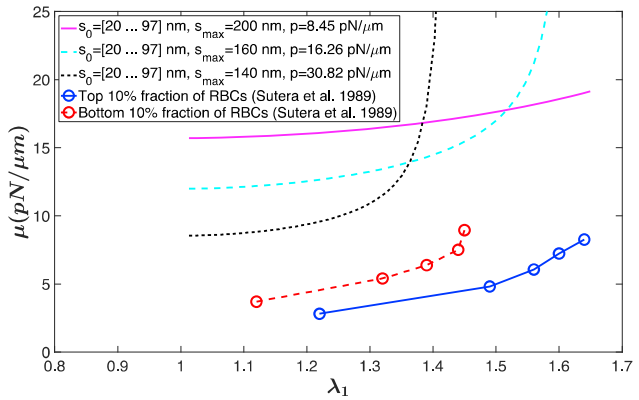

FIGURE 8 Shear modulus as a function of the principal stretch from the current model (area incompressible case) and tank-treading experiments. For the curves predicted from the model, parameters from the three cases in Fig. 7 *A* are used, and $\rho_0 = 2200/\mu m^2$. The shear modulus calculated from tank-treading motion of RBCs under shear is from (5). To see this figure in color, go online.

Dynamic remodeling, prestress of the spectrin network, and deformation mechanisms of spectrin

Prior studies considering the molecular basis of red cell membrane elasticity have introduced important potential attributes of the network that we do not consider here, namely dynamic remodeling of the network and the possibility of prestress of the skeleton in the resting state. For example, Fai et al. built a cytoskeletal network model based on cryo-EM tomography (10,18) and demonstrated that faster cytoskeletal reorganization leads to more irreversibly broken spectrin tetramers and a smaller dimensionless tank-treading frequency for a cell undergoing tank treading in shear flow. They also found that when the cell is placed under repeated strains, cytoskeletal dynamics may play a protective role by allowing spectrin tetramers to disconnect before they would break. Zhu and Asaro showed that the unfolding of spectrin can play a significant role in strain-softening of a spectrin network (40). Although these concepts are important considerations, Discher and colleagues report that there was no change in spectrin distribution in their fluorescence-imaged microdeformation experiments over periods of 30 min (15), indicating that if remodeling does occur, it does not have a substantial effect on the distribution of strain in deformed membranes over extended times. Therefore, we believe that our decision not to consider dynamic remodeling in micropipette experiments with much smaller extensions and shorter duration is justified.

It has long been recognized that the red cell membrane is a composite structure and that both the spectrin network and the lipid bilayer contribute to its overall mechanical behavior (1). For the analysis presented here, the bilayer is not expected to make substantial contributions, except to constrain the membrane to a constant surface area, because it offers no resistance to shear deformation, and its resistance to bending is small compared with the force resultants generated as a result of the network deformation during pipette aspiration (1). The composite nature of the red cell membrane, coupled with the very high resistance of the bilayer to surface dilation or compression, raises

the theoretical possibility that the skeleton itself may be slightly stretched or slightly compressed at rest, with the bilayer providing a counterbalance to make the net stress in the membrane zero at rest (41,42). The concept of a prestress in the spectrin network was introduced by Discher and colleagues to obtain agreement between their molecular-level red cell network simulations and experiments (9,43). More recently, we have identified a small adhesive energy between the membrane and the pipette surface that likely accounts for the discrepancy they observed for aspirations of biconcave cells (8), making the postulate of a skeletal prestress unnecessary for this case. (Predictions of the network density distribution in aspirated cells with long projections were also improved by inclusion of prestress, but this has not yet been addressed using the microstructure-based model we present here). The possibility of skeletal prestretch was also posited by Turlier et al. in a theory to explain how low-frequency cell fluctuations might be driven by spectrin because of changes in its phosphorylation state (44). Since then, a significant presence of myosin has been documented in red cells (45), which could provide an alternative explanation for the nonequilibrium, low-frequency fluctuations they observed. It could also be argued that long-term stress relaxation should cause network stress resultants to relax to zero over time. In summary, there is no clear evidence to confirm or refute the possibility that prestress may exist.

We consider each spectrin tetramer as a worm-like chain entropic spring in this study. Alternate models of spectrin behaving as a straight helical spring (46) or a Chinese finger trap (47), have been proposed. These models are based on electron micrographs of purified spectrin tetramers or mini-spectrins. Unfortunately, force-length relationships have not been derived for these cases. If such a force-length relationship existed, it would be straightforward to use the approach described here and incorporate it into our model by changing the potential in Eq. 2. Indeed, a similar approach to the one used here has been used with a model for spectrin as a helical spring to predict membrane behavior (8). That said, there are many experimental images of native spectrin in the actual RBC from quick-freeze, deep-etch, rotary replication procedure (48) or cryo-EM, in which the molecules appear to adopt random worm-like configurations (18), supporting the use of the worm-like chain potential not only here but in many theoretical and computational studies (10).

We note that the stiffening of the membrane at large extensions is reflected in both the thermodynamically defined shear modulus, μ, and the area modulus, K, both of which increase substantially with membrane dilation. It is also of interest that the value of the ratio K/μ also varies substantially from its resting value of 2.0, increasing with compression but decreasing for moderate extensions before increasing at very large extensions. Observations of the distribution of skeletal density in the projections of micropipette-aspirated cells indicated that this ratio should be $\sim$2.0, but a definitive value was not provided (15). This estimate of the K/μ ratio appears more or less consistent with the predictions of our model, but more detailed calculations would be required to draw a firm conclusion.

CONCLUSIONS

The work presented here makes several impactful contributions to our understanding of the physical basis of red blood cell membrane elasticity. First, we have derived a constitutive expression based on molecular properties that allows for local density changes in the deformed red cell cytoskeleton. We have generalized an expression for μ_0, the shear modulus for a network near the undeformed shape, previously derived for a network with just three chain orientations ($n = 3$) (7), and have shown that it is valid for arbitrary $n \geq 3$. Furthermore, we have developed the first, to our knowledge, molecularly based elastic model of the red blood cell membrane that accounts for both higher densities of spectrin indicated by proteomic analyses and distributed values of the resting molecular lengths obtained from electron-micrographic tomography. We have shown that for higher spectrin densities indicated by proteomics, accounting for a distribution of resting molecular lengths is essential for reproducing strain-hardening behavior exhibited by the red cell membrane in experiments. We have also obtained a relationship between the values for the maximal extended length of the spectrin tetramer and its persistence length that are consistent with membrane behavior in micropipette aspiration experiments. In addition, an analytical form of the micropipette aspiration with the simplified version of the constitutive law is derived. We find that the model exhibits hardening behavior and can help explain discrepancies found in the literature. In addition, this model can be also used to model other two-dimensional networks of flexible polymers with distributions of orientations and natural lengths, such as nuclear lamins.

SUPPORTING MATERIAL

Supporting Material can be found online at https://doi.org/10.1016/j.bpj.2020.10.025.

AUTHOR CONTRIBUTIONS

Z.P. and R.E.W. designed the research. Z.F., R.E.W., and Z.P. developed the mathematical models. R.E.W. performed the experiments. Z.F., R.E.W., and Z.P. analyzed the data. All authors contributed equally to writing the article.

ACKNOWLEDGMENTS

Z.F. and Z.P. acknowledge support from the National Science Foundation (grant no. 1706436-CBET).

REFERENCES

1. Evans, E. A., and R. Skalak. 1980. Mechanics and thermodynamics of biomembranes. CRC Press, Boca Raton FL.
2. Skalak, R., A. Tozeren, …, S. Chien. 1973. Strain energy function of red blood cell membranes. *Biophys. J.* 13:245–264.
3. Boal, D. 2012. Mechanics of the Cell, Second Edition. Cambridge University Press, Cambridge, UK.
4. Gerald Lim, H. W., M. Wortis, and R. Mukhopadhyay. 2008. Red blood cell shapes and shape transformations: Newtonian mechanics of a composite membrane: sections 2.5–2.8. *In* Soft Matter. G. Gompper and M. Schick, eds. Wiley-VCH Verlag GmbH & Co. KGaA, pp. 139–204.
5. Sutera, S. P., P. R. Pierre, and G. I. Zahalak. 1989. Deduction of intrinsic mechanical properties of the erythrocyte membrane from observations of tank-treading in the rheoscope. *Biorheology.* 26: 177–197.
6. Dimitrakopoulos, P. 2012. Analysis of the variation in the determination of the shear modulus of the erythrocyte membrane: effects of the constitutive law and membrane modeling. *Phys. Rev. E Stat. Nonlin. Soft Matter Phys.* 85:041917.
7. Dao, M., J. Li, and S. Suresh. 2006. Molecularly based analysis of deformation of spectrin network and human erythrocyte. *Mat. Sci. Eng. C.* 26:1232–1244.
8. Svetina, S., G. Kokot, …, R. E. Waugh. 2016. A novel strain energy relationship for red blood cell membrane skeleton based on spectrin stiffness and its application to micropipette deformation. *Biomech. Model. Mechanobiol.* 15:745–758.
9. Discher, D. E., D. H. Boal, and S. K. Boey. 1998. Simulations of the erythrocyte cytoskeleton at large deformation. II. Micropipette aspiration. *Biophys. J.* 75:1584–1597.
10. Fai, T. G., A. Leo-Macias, …, C. S. Peskin. 2017. Image-based model of the spectrin cytoskeleton for red blood cell simulation. *PLoS Comput. Biol.* 13:e1005790.
11. Li, J., M. Dao, …, S. Suresh. 2005. Spectrin-level modeling of the cytoskeleton and optical tweezers stretching of the erythrocyte. *Biophys. J.* 88:3707–3719.
12. Bryk, A. H., and J. R. Wiśniewski. 2017. Quantitative analysis of human red blood cell proteome. *J. Proteome Res.* 16:2752–2761.
13. Gautier, E.-F., M. Leduc, …, P. Mayeux. 2018. Absolute proteome quantification of highly purified populations of circulating reticulocytes and mature erythrocytes. *Blood Adv.* 2:2646–2657.
14. Burton, N. M., and L. J. Bruce. 2011. Modelling the structure of the red cell membrane. *Biochem. Cell Biol.* 89:200–215.
15. Discher, D. E., N. Mohandas, and E. A. Evans. 1994. Molecular maps of red cell deformation: hidden elasticity and in situ connectivity. *Science.* 266:1032–1035.
16. Boey, S. K., D. H. Boal, and D. E. Discher. 1998. Simulations of the erythrocyte cytoskeleton at large deformation. I. Microscopic models. *Biophys. J.* 75:1573–1583.
17. Marko, J. F., and E. D. Siggia. 1995. Stretching DNA. *Macromolecules.* 28:8759–8770.
18. Nans, A., N. Mohandas, and D. L. Stokes. 2011. Native ultrastructure of the red cell cytoskeleton by cryo-electron tomography. *Biophys. J.* 101:2341–2350.
19. Pan, L., R. Yan, …, K. Xu. 2018. Super-resolution microscopy reveals the native ultrastructure of the erythrocyte cytoskeleton. *Cell Rep.* 22:1151–1158.
20. Waugh, R. E., and P. Agre. 1988. Reductions of erythrocyte membrane viscoelastic coefficients reflect spectrin deficiencies in hereditary spherocytosis. *J. Clin. Invest.* 81:133–141.
21. Svoboda, K., C. F. Schmidt, …, S. M. Block. 1992. Conformation and elasticity of the isolated red blood cell membrane skeleton. *Biophys. J.* 63:784–793.
22. Stokke, B. T., A. Mikkelsen, and A. Elgsaeter. 1985. Human erythrocyte spectrin dimer intrinsic viscosity: temperature dependence and implications for the molecular basis of the erythrocyte membrane free energy. *Biochim. Biophys. Acta.* 816:102–110.
23. Cifra, P., Z. Benková, and T. Bleha. 2008. Persistence lengths and structure factors of wormlike polymers under confinement. *J. Phys. Chem. B.* 112:1367–1375.
24. Byers, T. J., and D. Branton. 1985. Visualization of the protein associations in the erythrocyte membrane skeleton. *Proc. Natl. Acad. Sci. USA.* 82:6153–6157.
25. Liu, S. C., L. H. Derick, and J. Palek. 1987. Visualization of the hexagonal lattice in the erythrocyte membrane skeleton. *J. Cell Biol.* 104:527–536.
26. Waugh, R., and E. A. Evans. 1979. Thermoelasticity of red blood cell membrane. *Biophys. J.* 26:115–131.
27. Chien, S., K. L. Sung, …, A. Tözeren. 1978. Theoretical and experimental studies on viscoelastic properties of erythrocyte membrane. *Biophys. J.* 24:463–487.
28. Hénon, S., G. Lenormand, …, F. Gallet. 1999. A new determination of the shear modulus of the human erythrocyte membrane using optical tweezers. *Biophys. J.* 76:1145–1151.
29. Lenormand, G., S. Hénon, …, F. Gallet. 2001. Direct measurement of the area expansion and shear moduli of the human red blood cell membrane skeleton. *Biophys. J.* 81:43–56.
30. Lenormand, G., S. Hénon, …, F. Gallet. 2003. Elasticity of the human red blood cell skeleton. *Biorheology.* 40:247–251.
31. Dao, M., C. T. Lim, and S. Suresh. 2003. Mechanics of the human red blood cell deformed by optical tweezers. *J. Mech. Phys. Solids.* 51:2259–2280.
32. Sleep, J., D. Wilson, …, W. Gratzer. 1999. Elasticity of the red cell membrane and its relation to hemolytic disorders: an optical tweezers study. *Biophys. J.* 77:3085–3095.
33. Fischer, T. M., C. W. Haest, …, R. Skalak. 1981. The stress-free shape of the red blood cell membrane. *Biophys. J.* 34:409–422.
34. Gerald Lim, H. W., M. Wortis, and R. Mukhopadhyay. 2002. Stomatocyte-discocyte-echinocyte sequence of the human red blood cell: evidence for the bilayer- couple hypothesis from membrane mechanics. *Proc. Natl. Acad. Sci. USA.* 99:16766–16769.
35. Omori, T., T. Ishikawa, …, T. Yamaguchi. 2011. Comparison between spring network models and continuum constitutive laws: application to the large deformation of a capsule in shear flow. *Phys. Rev. E Stat. Nonlin. Soft Matter Phys.* 83:041918.
36. Peterson, M. A., H. Strey, and E. Sackmann. 1992. Theoretical and phase contrast microscopic eigenmode analysis of erythrocyte flicker: amplitudes. *J. Phys. II.* 2:1273–1285.
37. Strey, H., M. Peterson, and E. Sackmann. 1995. Measurement of erythrocyte membrane elasticity by flicker eigenmode decomposition. *Biophys. J.* 69:478–488.
38. Tran-Son-Tay, R., S. P. Sutera, and P. R. Rao. 1984. Determination of red blood cell membrane viscosity from rheoscopic observations of tank-treading motion. *Biophys. J.* 46:65–72.
39. Drochon, A., D. Barthes-Biesel, …, J. C. Lelievre. 1990. Determination of the red blood cell apparent membrane elastic modulus from viscometric measurements. *J. Biomech. Eng.* 112:241–249.
40. Zhu, Q., and R. J. Asaro. 2008. Spectrin folding versus unfolding reactions and RBC membrane stiffness. *Biophys. J.* 94:2529–2545.
41. Boal, D. H., U. Seifert, and A. Zilker. 1992. Dual network model for red blood cell membranes. *Phys. Rev. Lett.* 69:3405–3408.
42. Peng, Z., X. Li, …, S. Suresh. 2013. Lipid bilayer and cytoskeletal interactions in a red blood cell. *Proc. Natl. Acad. Sci. USA.* 110:13356–13361.
43. Discher, D. E. 2000. New insights into erythrocyte membrane organization and microelasticity. *Curr. Opin. Hematol.* 7:117–122.
44. Turlier, H., D. A. Fedosov, …, T. Betz. 2016. Equilibrium physics breakdown reveals the active nature of red blood cell flickering. *Nat. Phys.* 12:513–519.

45. Smith, A. S., R. B. Nowak, …, V. M. Fowler. 2018. Myosin IIA interacts with the spectrin-actin membrane skeleton to control red blood cell membrane curvature and deformability. *Proc. Natl. Acad. Sci. USA.* 115:E4377–E4385.

46. McGough, A. M., and R. Josephs. 1990. On the structure of erythrocyte spectrin in partially expanded membrane skeletons. *Proc. Natl. Acad. Sci. USA.* 87:5208–5212.

47. Brown, J. W., E. Bullitt, …, C. J. McKnight. 2015. The physiological molecular shape of spectrin: a compact supercoil resembling a Chinese finger trap. *PLoS Comput. Biol.* 11:e1004302.

48. Ursitti, J. A., D. W. Pumplin, …, R. J. Bloch. 1991. Ultrastructure of the human erythrocyte cytoskeleton and its attachment to the membrane. *Cell Motil. Cytoskeleton.* 19:227–243.

Biophysical Journal, Volume *119*

Supplemental Information

Constitutive Model of Erythrocyte Membranes with Distributions of Spectrin Orientations and Lengths

Zhe Feng, Richard E. Waugh, and Zhangli Peng

APPENDIX A. Numerical solution of pipette aspiration using an ODE model

The deformation of the aspirated cell is assumed to be radially symmetric. An initial resting state is defined as a biconcave disc according to the formulations of Fung (1)

$$z(r) = (c_0 + c_1 {r_0}^2 + c_2 {r_0}^4)\sqrt{1 - (r_0/R_0)^2} \tag{S1}$$

where z is the half thickness of the cell, r_0 is the radial coordinate, and R_0 is the cell radius. (Note, the subscript "0" indicates that this is the radial position of a material element in the undeformed shape.) This expression is integrated to obtain the distance along the surface, $s_0(r_0)$, and the area of the surface inside the coordinate value $A_0(r_0)$. This information is saved in a look-up table for determination of r_0 for a given A_0. (Note that once the integration passes the edge of the undeformed cell, the relevant area is the area of one half of the cell plus the area outside the coordinate value r_0.)

To solve for the distribution of stress and density on the deformed surface we integrate the tangential force balance as

$$\frac{\partial \tau_1^{sk}}{\partial s} = -\frac{1}{r}\left(\tau_1^{sk} - \tau_2^{sk}\right)\cos(\theta) \tag{S2}$$

where s is the distance along the surface of the deformed shape, r is the radial coordinate of the deformed shape τ_1^{sk} and τ_2^{sk} are the meridional and the circumferential principal force resultants, and θ is the angle between the surface normal and the axis of symmetry ($\cos\theta = \mathrm{d}r/\mathrm{d}s$). The integration must be completed under the constraint that the mass of membrane skeleton is constant

$$\oint \rho dA = \oint \rho\, 2\pi r ds = \oint \rho_0 dA_0 \tag{S3}$$

Note that the resting density ρ_0 is assumed to be constant and that $\rho/\rho_0 = 1/(\lambda_1\lambda_2)$. The constraint can be written as

$$\oint \frac{\rho}{\rho_0}\, 2\pi r ds = A_0 \tag{S4}$$

This relationship is also the basis for determining r_0, the radial position of the instantaneous material element in the undeformed state. This is needed to calculate $\lambda_2 = r/r_0$. Therefore, we use the fact that

$$\frac{\mathrm{d}A_0}{\mathrm{d}s} = \frac{2\pi r}{\lambda_1 \lambda_2} \tag{S5}$$

and use the look-up table constructed from the unstressed geometry to find $r_0(A_0)$. The integration of the tangential force balance proceeds with s as the independent variable. The shape of the surface is assumed to be known: a hemispherical cap radius R_p, a section of cylinder with radius R_p and length L_p - R_p, and a biconcave shape described by Eq. S1 with the maximum radius calculated to maintain the total area of the shape a constant

$$2\pi {R_p}^2 + 2\pi R_p\left(L_p - R_p\right) + A_{disk} = A_0 \tag{S6}$$

Because the shape is fixed, for any s, the radius r and the angle to the surface normal θ are known. It is fairly straightforward to integrate the three simultaneous first order differential equations for the dependent variables A_0 and τ_1.

Starting the integration at the tip of the pipette, a guess is made for the starting value of $\lambda_o = \lambda_1 = \lambda_2$ at the tip. One approach is to use this starting value to integrate over the entire cell surface and adjust the value of λ_o in repeated tries until the mass conservation condition is met. This approach is problematic because of singularities that occur when λ_o is too small and the integrated value of A_0 is smaller than the cell area. In this case r_o goes to zero, and λ_2 becomes infinite. A more robust approach is to choose a location (for example the base of the projection at the edge of the pipette), and calculate two sets of solution values for A_0 and τ_1 at the chosen location, one starting from the tip of the projection for a range of starting values for λ_o, and one starting at the

opposite pole at the center of the disk for a range of starting values λ_d. If we let the integrated A_0 on the disk be A_{0d}, and the integrated A_0 of the projection be A_{0p}, then we require that

$$A_0 - A_{0d} = A_{0p} \tag{S7}$$

We can then plot two curves, one of (A_0 - A_{0d}) as a function of τ_1^{sk} (or equivalently, λ_1) at $r = R_p$ determined from the disk integration, and one of A_{0p} as a function of τ_1^{sk} (or equivalently, λ_1) at the base of the projection from the integration over the projection. The solution occurs where these two curves cross. The corresponding values for λ_o and λ_d are the starting values for the solution satisfying continuity of stress and mass conservation over the cell surface. Curves showing the solution intersections for a series of projection lengths is shown in Figure S1, and the distribution of density and shear force resultant are shown in Figures S2 and S3. The distribution of the principal stretch ratios is shown in Figure S4. The reader is advised that this method is not efficient, and may require significant computing time, particularly for cases where the values of initial molecular lengths are distributed.

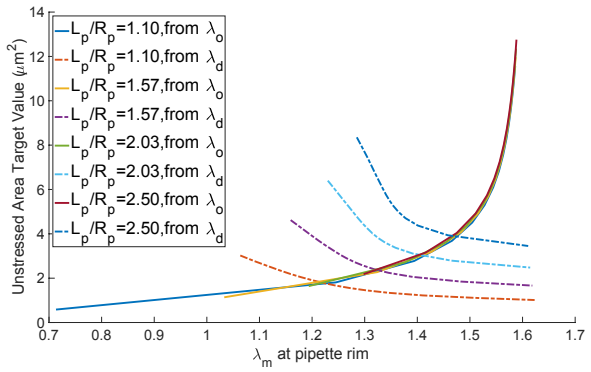

Figure S1. Intersecting curves show the solution points for four cases of increasing Lp/Rp. The four curves for the disk solutions overlap, and the four sets of solutions for the projections are labeled as shown.

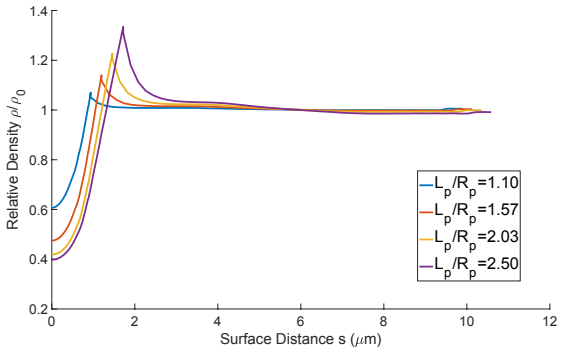

Figure S2. Distribution of density relative to the resting density ρ_0 over the surface of the cell. The distance s is measured along the surface from the tip of the projection.

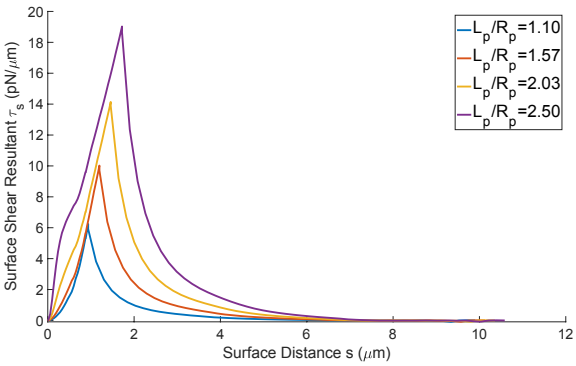

Figure S3. Distribution of the shear force resultant τ_s over the surface of the cell. The distance s is measured along the surface from the tip of the projection.

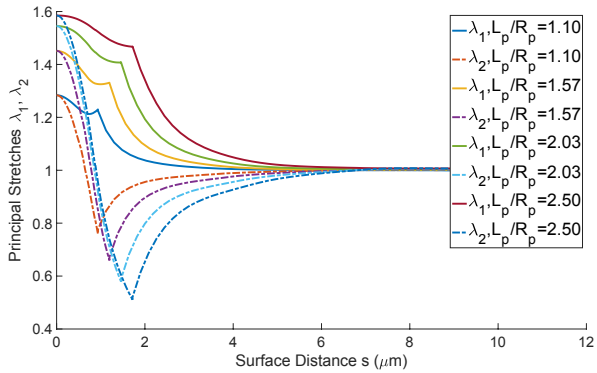

Figure S4. Distribution of the principal stretches over the surface of the cell. The distance s is measured along the surface from the tip of the projection.

APPENDIX B. Detailed derivations of the constitutive models

Derivation of the simplified constitutive model

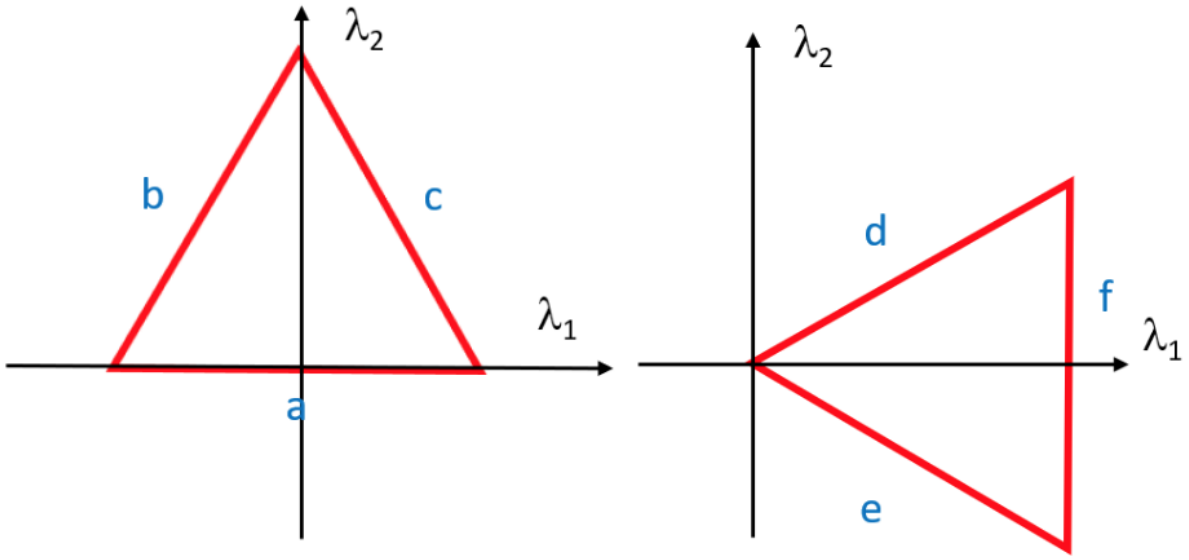

Figure S5. Network elements having six different molecular orientations in the resting state. Directions of the principle stretch directions are as shown. Letters of the segments correspond to those in the energy expression (Eq. S8).

For a unit cell with two orientations shown in Figure S5, i.e. $n = 6$, the free energy density is:

$$\begin{aligned} w &= \frac{1}{4A_0}V_{WLC}(a) + 2V_{WLC}(b) + V_{WLC}(f) + 2V_{WLC}(d) + \frac{C}{4A} \\ &= \frac{2c_\beta}{3x_0^2}\left[\frac{3\lambda_1^2x_0^2 - 2\lambda_1^3x_0^3}{2-2\lambda_1x_0} + \frac{3(\lambda_1^2+3\lambda_2^2)x_0^2 - (\lambda_1^2+3\lambda_2^2)^{3/2}x_0^3}{1-\sqrt{\frac{\lambda_1^2}{4}-\frac{3\lambda_2^2}{4}}x_0}\right. \\ &\left. + \frac{3\lambda_2^2x_0^2 - 2\lambda_2^3x_0^3}{2-2\lambda_2x_0} + \frac{3(\lambda_2^2+3\lambda_1^2)x_0^2 - (\lambda_2^2+3\lambda_1^2)^{3/2}x_0^3}{1-\sqrt{\frac{\lambda_2^2}{4}-\frac{3\lambda_1^2}{4}}x_0}\right] + \frac{C}{4A} \end{aligned} \tag{S8}$$

where $c_\beta = \frac{k_BT\rho_0s_0}{8p\lambda_{max}} = \frac{\sqrt{3}k_BT}{4ps_{max}}$, and the principal stress resultants are given by Eq. 5 and Eq. 6 as

$$\tau_1^{sk} = \frac{4c_\beta}{3}\frac{\lambda_1}{\lambda_2}\left[\frac{\frac{1}{4(1-\lambda_1 x_0)^2} + \lambda_1 x_0 - \frac{1}{4}}{\lambda_1 x_0} + \frac{\frac{1}{4\left(1-\sqrt{\frac{\lambda_1^2}{4}+\frac{3\lambda_2^2}{4}}x_0\right)^2} + \lambda_1 x_0 - \frac{1}{4}}{\sqrt{\frac{\lambda_1^2}{4}+\frac{3\lambda_2^2}{4}}x_0}\frac{1}{2}\right.$$
$$\left. + \frac{\frac{1}{4\left(1-\sqrt{\frac{\lambda_2^2}{4}+\frac{3\lambda_1^2}{4}}x_0\right)^2} + \lambda_1 x_0 - \frac{1}{4}}{\sqrt{\frac{\lambda_2^2}{4}+\frac{3\lambda_1^2}{4}}x_0}\frac{3}{2}\right] - \frac{c_\beta c_\alpha}{\lambda_1^2\lambda_2^2} \quad (S9)$$

$$\tau_2^{sk} = \frac{4c_\beta}{3}\frac{\lambda_2}{\lambda_1}\left[\frac{\frac{1}{4(1-\lambda_2 x_0)^2} + \lambda_2 x_0 - \frac{1}{4}}{\lambda_2 x_0} + \frac{\frac{1}{4\left(1-\sqrt{\frac{\lambda_2^2}{4}+\frac{3\lambda_1^2}{4}}x_0\right)^2} + \lambda_1 x_0 - \frac{1}{4}}{\sqrt{\frac{\lambda_1^2}{4}+\frac{3\lambda_2^2}{4}}x_0}\frac{1}{2}\right.$$
$$\left. + \frac{\frac{1}{4\left(1-\sqrt{\frac{\lambda_2^2}{4}+\frac{3\lambda_1^2}{4}}x_0\right)^2} + \lambda_1 x_0 - \frac{1}{4}}{\sqrt{\frac{\lambda_1^2}{4}+\frac{3\lambda_2^2}{4}}x_0}\frac{3}{2}\right] - \frac{c_\beta c_\alpha}{\lambda_1^2\lambda_2^2} \quad (S10)$$

The shear stress, mean stress, shear modulus, and area modulus are given as

$$\tau_s^{sk} = \frac{\tau_1^{sk} - \tau_2^{sk}}{2} = \frac{1}{2}\left(\frac{\partial w}{\partial \lambda_1}\frac{1}{\lambda_2} - \frac{\partial w}{\partial \lambda_2}\frac{1}{\lambda_1}\right) \quad (S11)$$

$$\tau_a^{sk} = \frac{\tau_1^{sk} + \tau_2^{sk}}{2} = \frac{1}{2}\left(\frac{\partial w}{\partial \lambda_1}\frac{1}{\lambda_2} + \frac{\partial w}{\partial \lambda_2}\frac{1}{\lambda_1}\right) \quad (S12)$$

$$\mu = \left|\frac{2\tau_s^{sk}\lambda_1^2\lambda_2^2}{\lambda_1^2 - \lambda_2^2}\right| \quad (S13)$$

$$K = \frac{\partial \tau_a}{\partial \alpha} = \frac{\partial^2 w}{\partial \alpha^2} \quad (S14)$$

$$\tau_s^{sk} = \frac{2c_\beta}{3\lambda_1\lambda_2}\left[\frac{\frac{1}{4(1-\lambda_1 x_0)^2}+\lambda_1 x_0-\frac{1}{4}}{\lambda_1 x_0}\lambda_1^2 - \frac{\frac{1}{4(1-\lambda_2 x_0)^2}+\lambda_2 x_0-\frac{1}{4}}{\lambda_2 x_0}\lambda_2^2\right.$$
$$+\frac{\frac{1}{4\left(1-\sqrt{\frac{\lambda_1^2}{4}+\frac{3\lambda_2^2}{4}}x_0\right)^2}+\lambda_1 x_0-\frac{1}{4}}{\sqrt{\frac{\lambda_1^2}{4}+\frac{3\lambda_2^2}{4}}x_0}\left(\frac{\lambda_1^2}{2}-\frac{3\lambda_2^2}{2}\right)+\frac{\frac{1}{4\left(1-\sqrt{\frac{\lambda_2^2}{4}+\frac{3\lambda_1^2}{4}}x_0\right)^2}+\lambda_1 x_0-\frac{1}{4}}{\sqrt{\frac{\lambda_2^2}{4}+\frac{3\lambda_1^2}{4}}x_0}\left(\frac{3\lambda_1^2}{2}-\frac{\lambda_2^2}{2}\right) \quad \text{(S15)}$$

$$\tau_a^{sk} = \frac{2c_\beta}{3\lambda_1\lambda_2}\left[\frac{\frac{1}{4(1-\lambda_1 x_0)^2}+\lambda_1 x_0-\frac{1}{4}}{\lambda_1 x_0}\lambda_1^2 + \frac{\frac{1}{4(1-\lambda_2 x_0)^2}+\lambda_2 x_0-\frac{1}{4}}{\lambda_2 x_0}\lambda_2^2\right.$$
$$+\frac{\frac{1}{4\left(1-\sqrt{\frac{\lambda_1^2}{4}+\frac{3\lambda_2^2}{4}}x_0\right)^2}+\lambda_1 x_0-\frac{1}{4}}{\sqrt{\frac{\lambda_1^2}{4}+\frac{3\lambda_2^2}{4}}x_0}\left(\frac{\lambda_1^2}{2}+\frac{3\lambda_2^2}{2}\right)$$
$$\left.+\frac{\frac{1}{4\left(1-\sqrt{\frac{\lambda_2^2}{4}+\frac{3\lambda_1^2}{4}}x_0\right)^2}+\lambda_1 x_0-\frac{1}{4}}{\sqrt{\frac{\lambda_2^2}{4}+\frac{3\lambda_1^2}{4}}x_0}\left(\frac{3\lambda_1^2}{2}+\frac{\lambda_2^2}{2}\right)\right] - \frac{c_\beta c_\alpha}{(\lambda_1\lambda_2)^2} \quad \text{(S16)}$$

To simplify the stress expressions, we explore the fact that Eq. 3 is an interpolation formula to the original worm-like chain model. In other words, Eq. 3 gives exact results for low and high force limits, but only gives an approximate result in intermediate force range (15% relative error). To obtain a simplified strain energy function, we will make it exact for low and high force limits, but construct an interpolation formula of stress in terms of stretches rather than the force in terms of chain length *s* in Eq. 3.

Simplified constitutive model with area change

To simplify the expression of the shear stress resultant in Eq. S15, assume it can be approximated as the following interpolated forms

$$\tau_{ss}^{sk} = \frac{2c_\beta}{3x_0}[d_0 + d_1(\lambda_s - 1) + \frac{d_\infty \lambda_s}{(1 - \lambda_s\lambda_a x_0)^2}] \quad (S17)$$

where the deformation is expressed in terms of isotropic (λ_a) and shear (λ_s) coefficients $\lambda_a = \sqrt{\lambda_1\lambda_2} = \sqrt{\alpha + 1}$, $\lambda_s = \sqrt{\lambda_1/\lambda_2}$.

To determine the three coefficients (d_0, d_1, d_∞) we match the slope of Eq. 18 with Eq. 10 with n = 6 for the low force limit and the high force limit.

At the high force limit, $\lambda_s\lambda_a x_0 \sim 1$, where the protein chain is close to its contour length, with asymptotic expansion at the high force limit or Laurent expansion, we get:

$$\tau_s^{sk} \sim \frac{2c_\beta}{3x_0\lambda_a^2}\left[\frac{\lambda_a\lambda_s}{4(1 - \lambda_s\lambda_a x_0)^2} + O(1)\right] \quad (S18)$$

At the same time the simplified shear stress near the high force limit:

$$\tau_{ss}^{sk} \sim \frac{2c_\beta}{3x_0}\left[\frac{d_\infty \lambda_s}{(1 - \lambda_s\lambda_a x_0)^2} + O(1)\right]$$

By matching them we can get

$$d_\infty = \frac{1}{4\lambda_a} \quad (S19)$$

Enforcing $\tau_s^{sk} = 0\ for\ \lambda_s = 1$,which means no shear stress when there is no shear deformation, we found that:

$$\tau_{ss}^{sk} = \frac{2c_\beta}{3x_0}\left[d_0 + \frac{d_\infty}{(1 - \lambda_a x_0)^2}\right] = 0 \quad (S20)$$

so

$$d_0 = \frac{-1}{4\lambda_a x_0^2(\lambda_a - 1/x_0)^2}, \quad (S21)$$

We obtain d_1 by matching slopes in terms of λ_s near $\lambda_s = \lambda_a = 1$,which is equivalent to matching the initial shear modulus μ_0. At the low shear force point, where there is no shear

deformation,

$$\mu = \frac{2\tau_{ss}^{sk}\lambda_1^2\lambda_2^2}{\lambda_1^2-\lambda_2^2}\bigg|_{\lambda_s\to 1} = \frac{c_\beta}{3x_0}\left[\frac{1+\lambda_a x_0}{4\lambda_a(1-\lambda_a x_0)^3} + d_1(\lambda_a x_0)\right]$$

Assuming the shear modulus under area deformation is only a function of expanded chain length $\lambda_a x_0$,

$$\mu = \mu(\lambda_a x_0),$$

which indicates $\frac{c_\beta}{3x_0} d_1 = f(\lambda_a x_0)$ is also a function of $\lambda_a x_0$. This means that during area expansion, the shear modulus hardening is independent of s_0 and depends only on the expanded chain length $\lambda_a s_0$. Then we have

$$\mu_0 = c_\beta\left(c_\alpha + \frac{3x_0 - x_0^2}{4(1-x_0)^3}\right) = \frac{c_\beta}{3x_0}\left[\frac{1+x_0}{4(1-x_0)^3} + d_1(x_0)\right]$$

$$\frac{d_1(x_0)}{x_0} = \frac{48(x_0)^4 - 153(x_0)^3 + 171(x_0)^2 - 71(x_0) + 1}{4x_0(x_0-1)^3},$$

then:

$$\frac{d_1(\lambda_a x_0)}{x_0} = \frac{48(\lambda_a x_0)^4 - 153(\lambda_a x_0)^3 + 171(\lambda_a x_0)^2 - 71(\lambda_a x_0) + 1}{4\lambda_a x_0(\lambda_a x_0 - 1)^3} \qquad (S22)$$

So

$$d_1 = \frac{48(\lambda_a x_0)^4 - 153(\lambda_a x_0)^3 + 171(\lambda_a x_0)^2 - 71(\lambda_a x_0) + 1}{4\lambda_a(\lambda_a x_0 - 1)^3} \qquad (S23)$$

Although the above equations were derived from the case of $n = 6$, it works for arbitrary $n > 2$, assuming isotropy.

If the area is incompressible, our formulation is reduced to

$$\tau_s^{sk} = \frac{2c_\beta}{3x_0}\left[c_0 + c_1(\lambda_1 - 1) + \frac{\lambda_1}{4(1-\lambda_1 x_0)^2}\right] \qquad (S24)$$

where $c_0 = \frac{-1}{4(1-x_0)^2}$

$$c_1 = \frac{48{x_0}^4 - 153{x_0}^3 + 171{x_0}^2 - 71x_0 + 1}{4(x_0 - 1)^3}$$

$$\mu = \frac{2\tau_s^{sk}}{\lambda_1^2 - \lambda_2^2} = \frac{4c_\beta}{3x_0(\lambda_1^2 - \lambda_2^2)}\left[c_0 + c_1(\lambda_1 - 1) + \frac{\lambda_1}{4(1-\lambda_1 x_0)^2}\right] \quad (S25)$$

This equation also works for arbitrary n>2.

Finite thermoelasticity and stresses of 2D hyperelastic membranes

Let's consider the cytoskeletal network as a 2D hyperelastic material without any remodeling or dissipation. The Cauchy stress of a hyperelastic material is given as

$$\boldsymbol{\sigma} = \frac{2}{J}\boldsymbol{F}\frac{\partial w}{\partial \boldsymbol{C}}\boldsymbol{F}^T \quad (S26)$$

where $w = H\text{-}TS = w(\boldsymbol{F},T)$ is the free energy density (measured per unit volume), $\boldsymbol{C} = \boldsymbol{F^T F}$ is the right Cauchy-Green deformation tensor, **F** is the deformation gradient, and $J = det(\mathbf{F})$. H is the enthalpy (internal energy, per unit volume), T is the temperature, and S is the entropy (per unit volume). If the material is isotropic, invariants of the deformation can be used to simplify the stress expression, so that the Cauchy stress resultant of a 2D isotropic hyperelastic material in Eq. S26 is reduced to

$$\boldsymbol{\tau} = \boldsymbol{\sigma}h = \tau_a \boldsymbol{I} + \frac{\mu}{(\alpha+1)^2}\left(\boldsymbol{B} - \frac{\mathrm{trace}(\boldsymbol{B})}{2}\boldsymbol{I}\right) \quad (S27)$$

where

$$\tau_a = \frac{\partial \mathrm{w}}{\partial \alpha}, \mu = \frac{\partial \mathrm{w}}{\partial \beta}, \boldsymbol{B} = \boldsymbol{F}\boldsymbol{F^T}, \boldsymbol{F} = \frac{\partial \mathbf{x}}{\partial \mathbf{X}}$$

where τ_α and μ are defined as the mean stress resultant and shear modulus and $\boldsymbol{B}$ is the left Cauchy-Green deformation tensor. The area invariant, $\alpha = \lambda_1\lambda_2 - 1$, and the shear invariant $\beta = (\lambda_1/\lambda_2 +$

λ_2/λ_1 - 2)/2 are those defined by Evans and Skalak (1), where λ_1 and λ_2 are the principal stretch ratios and h is the thickness. $\mathbf{x}$ is the current coordinate vector and $\mathbf{X}$ is the initial coordinate vector.

The principal stress resultants in the skeleton are related to the energy by:

$$\tau_1^{sk} = \frac{1}{\lambda_2}\frac{dw}{d\lambda_1} \tag{S28}$$

$$\tau_2^{sk} = \frac{1}{\lambda_1}\frac{dw}{d\lambda_2} \tag{S29}$$

To convert from the discrete form of the potential (expressed in terms of individual molecules) to a continuous form, the different deformation experienced by molecules having different orientations relative to the principal axes of deformation must be considered. We apply the affine assumption, namely, that the endpoints of the molecule follow the corresponding points in the continuum deformation. With this affine deformation assumption, we do not need to be concerned about the detailed connectivity between molecules. Taking s_o as the resting molecular length, the molecular extension (s/s_o) is related to the material extension ratios by

$$s^2 = \lambda_1^2 x_{0,i}^2 + \lambda_2^2 y_{0,i}^2$$

$$\left(\frac{s}{s_0}\right)_i^2 = \lambda_1^2\, cos^2\,\theta_{0,i} + \lambda_2^2\, sin^2\,\theta_{0,i} \tag{S30}$$

where $\theta_{0,i} = \frac{i\pi}{n}, i \in (1, n)$ is the angle between the molecular vector for orientation i and the principal axis of extension in the resting state. The energy per unit area must be summed over molecular orientations.

From Eq. 1 and. Eq. 2 we obtain

$$w_{total} = \sum_{i=1}^{n} V_{eff}(s)/A = \sum_{i=1}^{n} \frac{k_B T s_{max}}{4pA}\left(\frac{s}{s_{max}}\right)^2 \cdot \frac{3-2s/s_{max}}{1-s/s_{max}} cos^2\,\theta_{0,i}$$

Substituting this into Eq. S28 and Eq. S29 we arrive at

$$\tau_1^{sk} = \frac{1}{\lambda_2}\frac{dw}{d\lambda_1} = \frac{1}{\lambda_2}\frac{\partial w}{\partial s}\frac{\partial s}{\partial \lambda_1} = \frac{\lambda_1}{\lambda_2}\frac{\partial w}{\partial s}\frac{{s_0}^2}{s} cos^2\,\theta_{0,i}$$

$$= \sum_{i=1}^{n} \frac{k_B T}{4(p/s_0)A}\frac{\lambda_1}{\lambda_2}\left[\frac{1}{4(1-s/s_{max})^2} - \frac{1}{4} + s/s_{max}\right]\frac{s}{s_o} cos^2\,\theta_{0,i}$$

$$= \sum_{i=1}^{n} \frac{k_B T}{4(p/s_0)A\lambda_{max}}\frac{\lambda_1}{\lambda_2}\frac{6\lambda_{max}^2 - 9\lambda_{max}(s/s_o)_i + 4(s/s_o)_i^2}{(\lambda_{max} - (s/s_o)_i)^2} cos^2\,\theta_{0,i}$$

Since $\rho_0 = \frac{n}{A}$ in this case,

$$\tau_1^{sk} = c_\beta\left[\frac{2}{n}\frac{\lambda_1}{\lambda_2}\sum_{i=1}^{n}\left(cos^2\,\theta_{o,i}\cdot P_i\left(\frac{s}{s_o}\right)\right) - \frac{c_\alpha}{{\lambda_1}^2{\lambda_2}^2}\right] \quad \text{(S31)}$$

$$\tau_2^{sk} = c_\beta\left[\frac{2}{n}\frac{\lambda_2}{\lambda_1}\sum_{i=1}^{n}\left(sin^2\,\theta_{o,i}\cdot P_i\left(\frac{s}{s_o}\right)\right) - \frac{c_\alpha}{{\lambda_1}^2{\lambda_2}^2}\right] \quad \text{(S32)}$$

where

$$c_\alpha = \frac{6\lambda_{max}^2 - 9\lambda_{max} + 4}{(\lambda_{max} - 1)^2}$$

$$c_\beta = \frac{k_B T \rho_0}{8(p/s_0)\lambda_{max}}$$

and,

$$P_i(s/s_o) = \frac{6\lambda_{max}^2 - 9\lambda_{max}(s/s_o)_i + 4(s/s_o)_i^2}{(\lambda_{max} - (s/s_o)_i)^2}$$

Derivation of the area modulus K

For this 2D isotropic hyperelastic material, we can calculate the area modulus as:

$$K^{sk} \equiv \left(\frac{\partial \tau_\alpha^{sk}}{\partial \alpha}\right)_\beta \quad (S33)$$

with the stress expression

$$\tau_1^{sk} = c_\beta\left[\frac{2}{n}\frac{\lambda_1}{\lambda_2}\sum_{i=1}^{n}\left(cos^2\,\theta_{o,i}\cdot P_i\left(\frac{s}{s_o}\right)\right) - \frac{c_\alpha}{{\lambda_1}^2{\lambda_2}^2}\right],$$

$$\tau_2^{sk} = c_\beta \left[\frac{2}{n} \frac{\lambda_2}{\lambda_1} \sum_{i=1}^{n} \left(sin^2 \theta_{o,i} \cdot P_i \left(\frac{s}{s_o} \right) \right) - \frac{c_\alpha}{{\lambda_1}^2 {\lambda_2}^2} \right],$$

the tension can be calculated and simplified:

$$\tau_\alpha^{sk} = \frac{\tau_1^{sk} + \tau_2^{sk}}{2} = c_\beta \left[\frac{1}{n} \sum_{i=1}^{n} \left(\frac{\lambda_1}{\lambda_2} cos^2 \theta_{o,i} \cdot P_i \left(\frac{s}{s_o} \right) + \frac{\lambda_2}{\lambda_1} sin^2 \theta_{o,i} \cdot P_i \left(\frac{s}{s_o} \right) \right) - \frac{c_\alpha}{{\lambda_1}^2 {\lambda_2}^2} \right]$$

$$= c_\beta \left[\frac{1}{n\lambda_1\lambda_2} \sum_{i=1}^{n} (\lambda_1^2 cos^2 \theta_{0,i} + \lambda_2^2 sin^2 \theta_{0,i}) P_i \left(\frac{s}{s_o} \right) - \frac{c_\alpha}{{\lambda_1}^2 {\lambda_2}^2} \right]$$

$$= c_\beta \left[\frac{1}{n\lambda_1\lambda_2} \sum_{i=1}^{n} x^2 P_i(x) - \frac{c_\alpha}{{\lambda_1}^2 {\lambda_2}^2} \right] = c_\beta \left[\frac{1}{n(1+\alpha)} \sum_{i=1}^{n} x^2 P_i(x) - \frac{c_\alpha}{(1+\alpha)^2} \right] \quad (B34)$$

where $x_i^2 = \left(\frac{s}{s_0} \right)_i^2 = \lambda_1^2 cos^2 \theta_{0,i} + \lambda_2^2 sin^2 \theta_{0,i}$. From the expression of α and β in terms of λ_1 and λ_2, we can know:

$$\frac{\partial \lambda_1}{\partial \alpha} = \frac{1}{2\lambda_2}, \frac{\partial \lambda_2}{\partial \alpha} = \frac{1}{2\lambda_1} \quad (S35)$$

then $\frac{\partial x_i}{\partial \alpha}$ can be gained from Eq. S30

$$2x_i \frac{\partial x_i}{\partial \alpha} = 2\lambda_1 cos^2 \theta_{0,i} / (2\lambda_2) + 2\lambda_2 sin^2 \theta_{0,i} / (2\lambda_1)$$

$$\frac{\partial x_i}{\partial \alpha} = \lambda_1 cos^2 \theta_{0,i} / \lambda_2 + \lambda_2 sin^2 \theta_{0,i} / \lambda_1 = \frac{x_i^2}{2x_i\lambda_1\lambda_2} = \frac{x_i}{2(1+\alpha)} \quad (S36)$$

Also from Eq. 9, we have

$$\frac{\partial P_i(x)}{\partial x_i} = \frac{3\lambda_{max}^2 - \lambda_{max} x_i}{(\lambda_{max} - x_i)^3} \quad (S37)$$

Everything can be expressed in terms of α, therefore,

$$K = \partial c_\beta \left[\frac{1}{n(1+\alpha)} \sum_{i=1}^{n} x_i^2 P_i(x) \; - \; \frac{c_\alpha}{(1+\alpha)^2} \right] / \partial(\alpha)$$

$$= c_\beta \left[\frac{-1}{n(1+\alpha)^2} \sum_{i=1}^{n} {x_i}^2 P_i(x_i) \; + \frac{2}{n(1+\alpha)} \sum_{i=1}^{n} \frac{\partial x_i}{\partial \alpha} x_i P_i(x_i) \; + \frac{1}{n(1+\alpha)} \sum_{i=1}^{n} \frac{\partial x_i}{\partial \alpha} \frac{\partial P_i}{\partial x_i} {x_i}^2 \right.$$

$$\left. + \; \frac{2c_\alpha}{(1+\alpha)^3} \right]$$

$$= c_\beta \left[\frac{-1}{n(1+\alpha)^2} \sum_{i=1}^{n} {x_i}^2 P_i(x) \; + \frac{1}{n(1+\alpha)^2} \sum_{i=1}^{n} {x_i}^2 P_i(x) \; + \frac{1}{n(1+\alpha)} \sum_{i=1}^{n} \frac{\partial x_i}{\partial \alpha} \frac{\partial P_i}{\partial x_i} {x_i}^2 \; + \; \frac{2c_\alpha}{(1+\alpha)^3} \right] (S38)$$

So

$$K = c_\beta \left[\frac{1}{n(1+\alpha)} \sum_{i=1}^{n} \frac{x_i}{2(1+\alpha)} \frac{\partial P_i}{\partial x_i} {x_i}^2 + \; \frac{2c_\alpha}{(1+\alpha)^3} \right]$$

$$= \frac{c_\beta}{2n(1+\alpha)^2} \left[\sum_{i=1}^{n} {x_i}^3 \; \frac{3\lambda_{max}^2 - \lambda_{max} x}{(\lambda_{max} - x)^3} \right] + \; \frac{2c_\beta c_\alpha}{(1+\alpha)^3} \qquad (S39)$$

Two special cases of Eq. S39 are of interest. The first is the purely isotropic deformation (no shear). In this case $x = x_i = \lambda_1 = \lambda_2 = s_i/s_o = \lambda_{iso}$, and the expression reduces to:

$$K^{sk}|_{iso} = \frac{c_\beta}{2nx^4} \left[\sum_{i=1}^{n} x^3 \; \frac{3\lambda_{max}^2 - \lambda_{max} x}{(\lambda_{max} - x)^3} \right] + \; \frac{2c_\beta c_\alpha}{x^6} = \frac{c_\beta}{2x} \frac{3\lambda_{max}^2 - \lambda_{max} x}{(\lambda_{max} - x)^3} + \; \frac{2c_\beta c_\alpha}{x^6} \qquad (S40)$$

The second is the value for this coefficient in the resting state K_0^{sk}, i.e. in the limit as $x=\lambda_{iso} \rightarrow 1.0$:

$$K_0^{sk} = c_\beta \left(2c_\alpha + \frac{3\lambda_{max}^2 - \lambda_{max}}{2(\lambda_{max} - 1)^3} \right) \qquad (S41)$$

We can also derive an expression for the modulus μ for an isotopic deformation:

$$\mu_{iso} = c_\beta x^2 \left(\frac{6\lambda_{max}^2 - 9x\lambda_{max} + 4x^2}{(\lambda_{max} - x)^2} + \frac{x(3\lambda_{max}^2 - x\lambda_{max})}{4(\lambda_{max} - x)^3} \right) \quad (S42)$$

APPENDIX C. Analysis of micropipette aspiration with cytoskeletal area change

Here we consider the area change of the cytoskeleton when deriving the relationship between pressure and aspiration length in micropipette experiments. Assuming the area change of the cytoskeleton outside of the pipette is a uniform small constant α_0, the deformation can be obtained from the mass conservation and total area conservation as

$$\pi R_0^2 \rho_0 = \frac{\pi(r^2 - R_p^2)\rho_0}{1 + \alpha_0} + m_{inside} \quad (S43)$$

Since

$$\lambda_1 = \frac{(1 + \alpha_0)R_0}{r} \quad (S44)$$

then we have

$$\frac{dr}{d\lambda_1} = \frac{\lambda_1 r}{1 + \alpha_0 - \lambda_1^2} \quad (S45)$$

$$\tau_{1,tip}^{sk} = \int_{R_p}^{\infty} \frac{\left(\tau_1^{sk} - \tau_2^{sk}\right)dr}{r}$$
$$= \int_{\lambda_L}^{\sqrt{1+\alpha_0}} \frac{2\tau_s^{sk}}{r}\frac{dr}{d\lambda_1}d\lambda_1$$
$$= \int_{\lambda_L}^{\sqrt{1+\alpha_0}} \frac{4c_\beta}{3x_0}[d_0 + d_1(\lambda_s - 1) + \frac{d_\infty \lambda_s}{(1-\lambda_s\lambda_a x_0)^2}]\frac{\lambda_1}{1+\alpha_0-\lambda_1^2}d\lambda_1$$
$$= \int_{\lambda_L'}^{1} \frac{4c_\beta}{3x_0'}[d_0 + d_1(\lambda_s - 1) + \frac{d_\infty \lambda_s}{(1-\lambda_s\lambda_a x_0')^2}]\frac{\lambda_s}{1-\lambda_s^2}d\lambda_s$$
$$= \frac{4c_\beta}{3x_0'}\left[D_0' + D_1'\lambda_L' + D_2'\ln\left(\frac{\lambda_L'+1}{2}\right) + D_3'\ln\left(\frac{1-x_0'}{1-x_0'\lambda_L'}\right) + \frac{D_4'}{1-x_0'\lambda_L'}\right] \quad (S46)$$

Thus

$$R_p\Delta P = \frac{8c_\beta}{3x_0^{'}}\left[D_0^{'} + D_1^{'}\lambda_L^{'} + D_2^{'}\ln\left(\frac{\lambda_L^{'}+1}{2}\right) + D_3^{'}\ln\left(\frac{1-x_0^{'}}{1-x_0^{'}\lambda_L^{'}}\right) + \frac{D_4^{'}}{1-x_0^{'}\lambda_L^{'}}\right] + 2T_\infty \quad (S47)$$

where $\lambda_L^{'} = \lambda_L/\sqrt{\alpha_0+1}$ is the stretch at the entrance of pipette, and

$$D_0' = \frac{-1}{4(1+x_0')^2(1-x_0')^2x_0'} - c_1'$$

$$D_1^{'} = c_1^{'} = \frac{48x_0^{'4} - 153x_0^{'3} + 171x_0^{'2} - 71x_0^{'} + 1}{4\left(x_0^{'}-1\right)^3}$$

$$D_2^{'} = -\frac{x_0^{'2}+1}{4(1+x_0^{'})^2(1-x_0^{'})^2} - c_1^{'}$$

$$D_3^{'} = \frac{x_0^{'}}{2\left(1+x_0^{'}\right)^2\left(1-x_0^{'}\right)^2}$$

$$D_4^{'} = \frac{1}{4(1-x_0^{'})^2}$$

$$x_0^{'} = x_0\sqrt{1+\alpha_0}$$

$$\lambda_L^{'} = \frac{\sqrt{\frac{A_{cell}\alpha_0}{\pi} + 2R_pL_p}}{R_p}$$

where α_0 is the average area change of the flat membrane and $A_{cell} = 135\mu m^2$ is the surface area of the RBC. $T_\infty = K_0\alpha_0$, and K_0 is the initial area modulus of the cytoskeleton. We choose $K_0 = 2\mu_0$, since α_0 is small.

λ_L' is a function of α_0

By assuming the total membrane area is constant (A_{cell} = 135 μm^2) due to the total area constraints from lipid bilayer and the membrane outside of the pipette has a uniform small constant α_0, we have

$$\begin{aligned}
\text{Area conservation:} \quad & A_{cell} = 2\pi L_p R_p + A_{out}, \\
\text{Mass conservation:} \quad & \rho_0 A_{cell} = m_{inside} + \tfrac{A_{out}\rho_0}{\alpha_0+1}, \\
\text{Mass conservation:} \quad & \rho_0 A_{cell} = \rho_0 \pi \bar{R}_0^2 + \tfrac{A_{out}\rho_0}{\alpha_0+1},
\end{aligned}$$

A_{out} represents for the deformed membrane area outside of the pipette, m_{inside}/ρ_0 is the initial area of the membrane inside pipette.

By using A_{cell} = constant and eliminating A_{out}, we get

$$m_{inside} = \frac{A_{cell}\alpha_0 + 2\pi R_p L_p}{\alpha_0 + 1}\rho_0 \qquad (S48)$$

Since

$$\pi R_0^2 \rho_0 = \frac{\pi(r^2 - R_p^2)\rho_0}{1+\alpha_0} + m_{inside} \qquad (S49)$$

then

$$\pi R_0^2 = \frac{\pi(r^2 - R_p^2) + A_{cell}\alpha_0 + 2\pi R_p L_p}{1+\alpha_0} \qquad (S50)$$

In particular, if $r = R_p$, we have

$$\bar{R}_0^2 = R_0^2|_{r=R_p} = \frac{m_{inside}}{\pi\rho_0} = \frac{\frac{A_{cell}\alpha_0}{\pi} + 2R_pL_p}{\alpha_0 + 1} \quad (S51)$$

Since

$$\lambda_1 = \frac{(1+\alpha_0)R_0}{r}$$

we can solve λ_L as

$$\lambda_L = \frac{(1+\alpha_0)R_0}{r}\bigg|_{r=R_p} = \frac{\sqrt{\alpha_0+1}\sqrt{\frac{A_{cell}\alpha_0}{\pi} + 2R_pL_p}}{R_p} \quad (S52)$$

$$\lambda_L' = \lambda_L/\sqrt{\alpha_0+1} = \frac{\sqrt{\frac{A_{cell}\alpha_0}{\pi} + 2R_pL_p}}{R_p} \quad (S53)$$

APPENDIX D. Cytoskeletal area change and effect of the number of orientations

Additional details on stress-strain behavior: Area change with stretch

One important difference between uniaxial extension ($\tau_2 = 0$) and pure shear (constant area) is that the area of the skeleton does change with extension, as would be expected for a compressible material. This is illustrated in Fig. S6, where a biphasic change in skeletal area is predicted, increasing for smaller extensions and decreasing as the extension approaches λ_{max}. For small extensions, the corresponding change in area does not depend strongly on the maximum stretch ratios (Fig. S6A), but unlike the stress resultants at large extensions, the changes in area expressed as a function of the extension normalized to λ_{max} do not collapse to a single curve, but rather reflect larger area expansions for larger values of λ_{max} over the entire range of values (Fig. S6B).

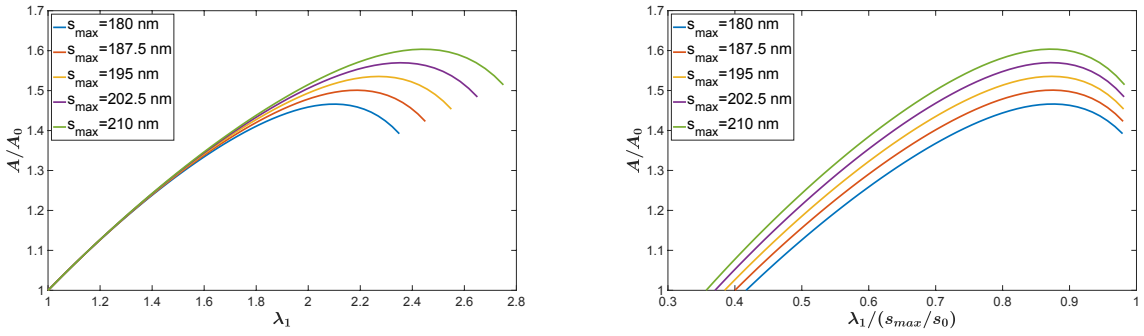

A. **B.**

Figure S6. A. The compressibility of the skeleton is reflected in increasing skeletal area with extension. Interestingly, the area increase reaches a maximum, and decreases at very high extensions. **B.** Unlike the stress resultant, the area change remains dissimilar for different values of λ_1/λ_{max} over the entire range of values. These curves reveal, however, that the maximum area increase occurs at approximately 86% of maximum extension for all λ_{max}.

Changes in shear modulus with area expansion

In Figure 2 of the manuscript we illustrate how the area modulus and the ratio of the area modulus change with membrane expansion. The shear modulus is also a function of both area

expansion and shear deformation. Both shear deformation (λ_1/λ_2) and skeletal dilation (α) cause molecules in the skeleton to approach their maximum length. Therefore, for larger ratios of λ_1/λ_2, the modulus approaches its asymptotic limit for smaller values of α. This is illustrated in Figure S7.

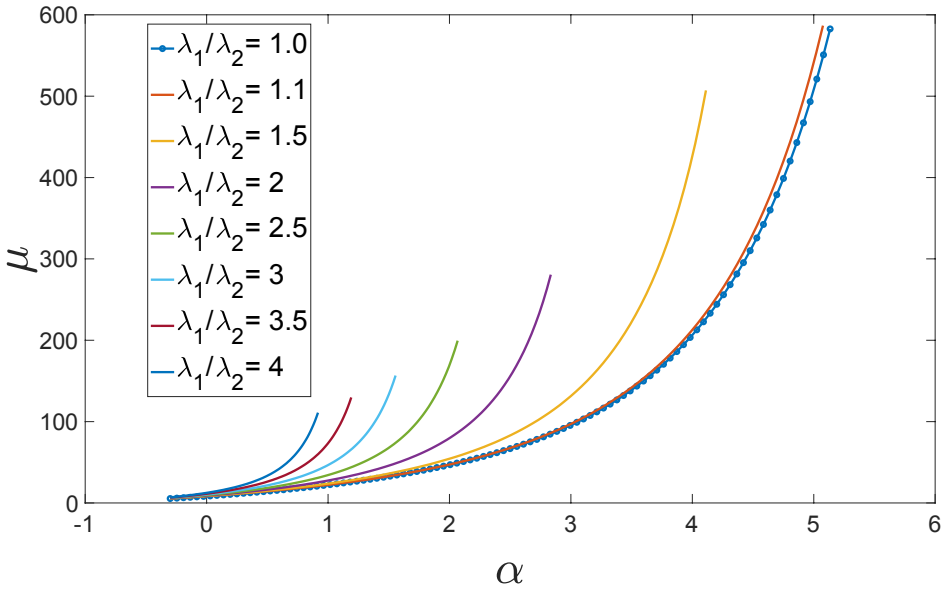

Figure S7. Dependence of the shear modulus on the area expansion for different ratios of stretches. The unit of the shear modulus is pN/ μm.

Increasing *n* to approximate a random network

Figure 2A in the main text shows how the calculated values of the stress resultant τ_1 vary with increasing n from 3 to 48. In this section we examine the dependence of the "error" introduced in calculating the stress resultant for different n, s_0 and s_{max}. For a given value of s_{max} the persistence length p is calculated according to the relationship given in the legend of Figure 7D:

$$p = c_1(6 - 9c_2/s_{max} + 4{c_2}^2/s_{max}^2)/(s_{max}/c_2 - 1)^2 \qquad (S54)$$

where $c_1 = 0.0275$ and $c_2 = 101.85$. We consider a simple uniaxial extension, both for the case of pure shear ($\lambda_2 = 1/\lambda_1$) and for the case $\tau_2 = 0$. As noted in the main text (Figure 2B), differences in calculated values of τ_1 for different n increase as the extension approaches $\lambda_{max} = s_0/s_{max}$. Therefore, we characterize the accuracy of the calculations in terms of the maximum extension of the material for which the difference in the calculated τ_1 is less than 1%. We find that this extension is within 0.5% of λ_{max} for all cases when comparing $n = 48$ with $n = 96$, indicating that $n = 48$ is a good approximation for $n \to \infty$. Therefore, the calculations were made for the maximum extension at which the calculated τ_1 is within 1% of the value calculated for $n = 48$.

We find that the maximum extensions for errors less than 1% depend on the specific value of s_0, but that the extensions expressed as a function of s_0/s_{max} fall on a single curve that is independent of s_{max} (Figure S8A). The maximum allowable extension increases with increasing n as expected (Figure S8B, Table S1). Similar results were obtained for pure shear deformations (Figures S8C and S8D). For modeling the skeleton with distributed values of s_0, we performed the weighted sum of contributions to τ_1 for the different values of s_0. The maximum allowable extensions for distributed values of s_0 are shown in Table S2. Note that when n is small ($n = 3$), significant errors can occur even for relatively modest extensions.

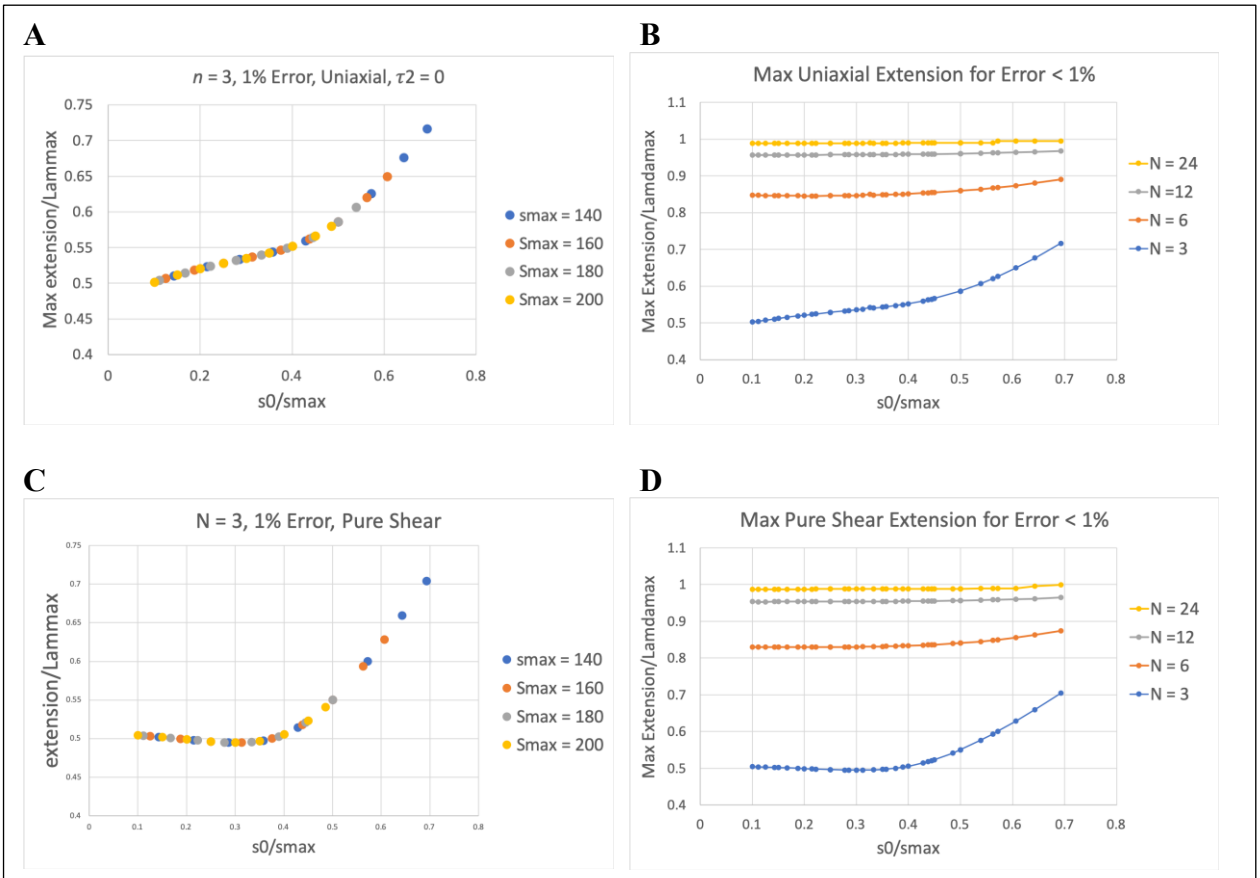

Figure S8. **A.** Maximum allowable extension for error < 1%, for uniaxial extension ($\tau_2 = 0$). When the extension and the values of s_0 are normalized by their maximum values, the curves are independent of s_{max}. **B.** The maximum allowable extension increases with increasing n. **C** and **D**. Similar results were obtained for pure shear deformation ($\lambda_2 = 1/\lambda_1$).

Table S1. Maximum allowable extension for 1% and 5% error (λ_1/λ_{max}, s_{max} = 180 nm)
Pure Shear

	1% error								
$n \setminus s_0$	20	30	40	50	60	70	80	90	97
3	0.5041	0.5012	0.4979	0.4953	0.4957	0.503	0.521	0.5502	0.5762
6	0.8298	0.8298	0.8298	0.8302	0.8312	0.833	0.8361	0.8407	0.8451
12	0.9532	0.9534	0.9534	0.9536	0.954	0.9545	0.9552	0.9564	0.9575
24	0.9874	0.9875	0.9876	0.9877	0.9878	0.988	0.9883	0.9886	0.9889
	5% error								
3	0.5785	0.5745	0.573	0.5686	0.5684	0.5685	0.5755	0.589	0.605
6	0.8677	0.8659	0.8686	0.8686	0.8668	0.8695	0.871	0.8744	0.8782
12	0.9656	0.9632	0.9649	0.9633	0.9654	0.9646	0.9671	0.9672	0.9671
24	0.9896	0.99	0.9905	0.9909	0.9914	0.9919	0.9924	0.9906	0.9911

Table S2. Maximum allowable extension (λ_1/λ_{max}, s_{max} = 180 nm), Uniaxial ($\tau_2 = 0$)

	1% error								
$n \setminus s_0$	20	30	40	50	60	70	80	90	97
3	0.5041	0.5149	0.5244	0.5323	0.54	0.5497	0.5645	0.5865	0.6065
6	0.8471	0.8458	0.8453	0.8459	0.8475	0.8503	0.8542	0.8594	0.8639
12	0.9569	0.9571	0.9571	0.9574	0.9579	0.9585	0.9593	0.9605	0.9614
24	0.9885	0.9886	0.9886	0.9888	0.9889	0.9891	0.9893	0.9896	0.9898
	5% error								
3	0.5963	0.5977	0.6046	0.6076	0.6132	0.6195	0.6277	0.6413	0.6522
6	0.8787	0.8799	0.8784	0.8813	0.882	0.884	0.8872	0.8896	0.8926
12	0.9662	0.9676	0.9692	0.9673	0.9692	0.9682	0.9704	0.9703	0.9700
24	0.9898	0.9902	0.9906	0.9911	0.9915	0.992	0.9925	0.993	0.9913

Table S3. Maximum allowable extension for distributed s_0 values, Pure Shear

s_{max}	200	180	160	140
λ_{max}	2.0619	1.8557	1.6495	1.4433
n	**Maximum allowable extension for error < 1%**			
3	1.31	1.20	1.11	1.05
6	1.84	1.66	1.48	1.31
12	1.99	1.79	1.59	1.40
24	2.04	1.84	1.63	1.43
	Maximum allowable extension for error < 5%			
3	1.47	1.33	1.20	1.09
6	1.89	1.71	1.52	1.34
12	2.00	1.81	1.61	1.41
24	2.04	1.84	1.64	1.43

Table S4. Maximum allowable extension for distributed s_0 values, Uniaxial ($\tau_2 = 0$)

s_{max} **(nm)**	200	180	160	140
λ_{max}	2.0619	1.8557	1.6495	1.4433
n	**Maximum allowable extension for error < 1%**			
3	1.41	1.29	1.18	1.09
6	1.86	1.68	1.50	1.33
12	1.99	1.80	1.60	1.41
24	2.04	1.84	1.64	1.43
	Maximum allowable extension for error < 5%			
3	1.56	1.42	1.28	1.15
6	1.91	1.72	1.53	1.35
12	2.01	1.81	1.61	1.41
24	2.05	1.84	1.64	1.43

Appendix E. Goodness of fit for different values of persistence length and maximum length.

Ideally one should be able to choose the best combination of molecular parameters (persistence length p and maximum molecular length s_{max}) based on the goodness of fit for the least squares regressions. Unfortunately, the resolution in the data is not sufficient to identify the best ordered pairs in the present case. The calculated sum of squared errors for each of the three different experiments presented in Figure 7 are tabulated below for the series of solution pairs for p and s_{max}. In two of the cases in Fig. 7, the lowest sum of squared errors occurs for small values of s_{max} and large values of p, but in the third case, the opposite is true. Which solution gives the lowest sum of squared errors depends critically on the data point at the highest pressure. Given this sensitivity, it would be inappropriate to infer too much about which of the possible combinations of s_{max} and p most accurately reflect true membrane properties.

Table S5 Fitting Error of Fig. 7A in the main text.

Smax	p	σ_{ap}	SSE	SSEp
130	48.5213	0.013069	0.99867	0.199734
135	37.12	1.07	1.122	0.2244
140	29.54	2.16	1.109	0.2218
145	24.19	3.38	0.911	0.1822
150	20.67	4.17	0.813	0.1626
160	15.54	6.28	0.674	0.1348
170	12.58	7.60	0.566	0.1132
180	10.61	8.74	0.498	0.0996
190	9.05	10.00	0.482	0.0964
200	8.03	10.64	0.4595	0.0919

R_p = 0.85 um. SSE: sum of the squared error. SSEp: sum of the squared error per data point.

Table S6 Fitting Error of Fig. 7B in the main text.

s_{max}	p	σ_{ap}	SSE	SSEp
130	52.3648	-3.4339	0.45421	0.090842
133	44.1032	-2.7385	0.37607	0.075214
135	39.8566	-2.3664	0.48052	0.096104
140	31.19	-0.89	0.5313	0.10626
145	26.26	-0.46	0.615	0.123
150	22.30	0.50	0.782	0.1564
160	16.71	2.56	1.083	0.2166
170	13.63	3.61	1.334	0.2668
180	11.39	4.80	1.54	0.308
190	9.82	5.77	1.948	0.3896
200	8.71	6.36	2.235	0.447

R_p = 0.55 um. SSE: sum of the squared error. SSEp: sum of the squared error per data point.

Table S7. Fitting Error of Fig. 7C in the main text.

s_{max}	p	σ_{ap}	SSE	SSEp
130	55.0781	-0.37773	3.5905	0.51292857
131	51.49	0	3.839	0.54842857
133	43.6	1.51	2.617	0.37385714
135	39.99	1.69	2.941	0.42014286
140	30.82	3.39	3.024	0.432
145	25.58	4.17	3.108	0.444
150	21.80	4.95	3.388	0.484
160	16.26	7.07	4.092	0.58457143
170	13.34	8.06	4.441	0.63442857
180	11.16	9.23	5.100	0.72857143
190	9.48	10.68	5.821	0.83157143
200	8.45	11.14	6.418	0.91685714

R_p = 0.55 um. SSE: sum of the squared error. SSEp: sum of the squared error per data point.

Supporting References.

1. Fung, Y. C., W. C. O. Tsang, and P. Patitucci. (1981). High-Resolution Data on the Geometry of Red-Blood-Cells. Biorheology 18(3-6):369-385.